NTNU

Norwegian University of
Science and Technology

Nanopositioning

Construction and Analysis of a Piezoelectric Tube Actuator

Even Vinge

Master of Science in Engineering Cybernetics
Submission date: June 2009
Supervisor: Jan Tommy Gravdahl, ITK

Norwegian University of Science and Technology
Department of Engineering Cybernetics

Problem Description

The topic of this thesis is nanopositioning using piezoelectric tube actuators. Atomic force microscopes (AFM) have enabled researchers to acquire precise images of samples down to atomic resolution, and are ubiquitous in several science fields. These scanning microscopes are limited in performance by several factors. One of these is the limited bandwidth of the scanning apparatus, most commonly implemented using piezoelectric tube actuators. Both linear and nonlinear properties of these actuators seem to limit the available bandwidth. Further research is required into this area in order to improve the capabilities of the actuators and subsequently the AFM.

The aim is to provide a complete laboratory setup for conducting experiments on piezoelectric tube actuators for use in AFM , and to analyze the properties of the actuators using the setup. The ultimate goal of the thesis is to lay the groundwork for continued research into the field of nanopositioning at NTNU.

1. Present the basic background and theory on AFM and specifically the piezoelectric tube actuator.

2. Design and build a laboratory setup for actuation and precise deflection measurement of a piezoelectric tube. You can use [1] as a reference for the setup when applicable.

3. Design a series of laboratory experiments to analyze important properties of the piezoelectric tube, and conduct these using the laboratory setup. The basic linear dynamics of the tube should be presented, as well as nonlinear effects that might affect the capabilities of the piezoelectric tube for use in AFM.

4. Compare and relate the results to existing literature on the subject, including [1].

[1] A. Fleming, A. Wills, and S. Moheimani, "Sensor fusion for improved control of piezoelectric tube scanners," Control Systems Technology, vol. 16, pp. 1265 – 1276, Nov 2008.

Co-supervisor: PhD student Arnfinn Aas Eielsen

Assignment given: 12. January 2009
Supervisor: Jan Tommy Gravdahl, ITK

Abstract

Piezoelectric tubes are commonly used as scanning actuators in nano precision microscopes. They can achieve precision down to sub-nanometer scale, but their vibrational dynamics and nonlinear properties hamper their ability to achieve higher bandwidths. In order to deal with this, further research is needed.

This thesis is a first look into the field of piezoelectric tube actuators, intended to lay the groundwork for further research on the subject at NTNU. It details the construction of a laboratory setup for actuation and nanometer displacement measurement of a piezoelectric tube.

Needed specifications are found and a mechanical setup is designed. Basic theory on piezoelectricity is presented, along with the setup and equipment used for the thesis.

Several experiments are designed and conducted in order to identify the linear dynamics and nonlinear properties of the piezoelectric tube. The results are discussed and related to current literature. This includes the linear frequency responses from applied voltage to displacement of the piezoelectric tube, noise levels and nonlinear properties such as displacement creep and hysteresis.

Generally, the results are found to closely match what has been found in similar research, although there are some notable differences, such as a somewhat smaller low frequency gain and a much lower resonant peak frequency of the system. Several possible explanations for these disparities are discussed.

Both a capacitive sensor and a piezoelectric strain voltage sensor are utilized for measuring displacement. It is found that the capacitive sensor has a higher noise level but is more accurate at lower frequencies than the strain voltage sensor. The two measurements are then combined into an improved estimate of the displacement of the piezoelectric tube.

Preface

This thesis concludes my Master's Degree in Engineering Cybernetics at NTNU. I've had five amazing years at NTNU, and I now feel prepared to take on the challenges that lie ahead. Especially during my work on this thesis I feel I've grown both academically and as a person, and there are several people who deserve credit for this.

First of all I would like to thank my supervisor, professor Jan Tommy Gravdahl, for great help and guidance with this thesis. I would also like to thank PhD candidate Arnfinn Aas Eielsen for his invaluable help in getting our lab set up and for his advice and insights during this last year. Thanks go out to to Stefano Bertelli, John Olav Horrigmo and Terje Haugen at ITK for their helpfulness. Without Terje's mechanical prowess the experiments conducted for this thesis wouldn't have been possible. Thanks are also due to fellow MSc students Christian Sesseng, Marit Owren, Ruben Ringset and Trond Tollefsen for valuable input in the research process.

To my dear friends Petter, Aleksander and Marie, you've made this last year a wonderful one, and I'm very grateful. Thanks for the many laughs, the needed distractions, the support and the motivation.

To my little brother Simen, you've always been a great inspiration to me and I look to you with admiration – keep up the good work.

And to mom and dad, for everything you have done, for your encouragement and for your unwavering confidence in me. I owe to you everything I'll ever become.

Contents

Chapter 1

Introduction

1.1 Motivation

Nanotechnology is the field of controlling and observing matter on the scale of atoms. This field has been the topic of much attention in scientific research the last decades, in many different disciplines.

Scanning probe microscopes (SPMs) have enabled researchers to record and visualize properties of samples down to atomic precision, and have become standard tools in many scientific fields.

These tools scan a sample in a raster pattern under a small probe, and record the forces measured by the probe related to position of the sample. The scanner used for this task is in in the majority of SPM and AFM setups implemented as a piezoelectric tube (in this thesis abbreviated PET) actuator.

PETs require significant power to generate the displacement needed for scanning, and their properties are dependent on several different factors such as scanning range and bandwidth. Much scientific progress has been made in analyzing and improving the properties of PET actuators. Especially the methods of cybernetics and control engineering have shown great promise in this field. The dynamics of the actuators have been modeled using various techniques, new methods of actuation and measurement have been applied, and control schemes have been designed to improve properties of PET actuators such as linearity and possible bandwidth.

A large share of this progress has been made in the last few years, and several research communities are still actively researching the properties of PETs. This suggests that there still are insights to be gained and improvements to be made by studying PET actuators.

This thesis is a first look into the field of PET actuators, intended to lay the groundwork for further research on the subject at NTNU. The hope is that the fruits of this thesis will be a continued research effort on the subject of nanopositioning in the years to come.

1.2 Contribution of this thesis

This thesis describes the construction of a simple PET actuator, including methods and instruments for actuating the PET and for measuring the resulting displacement down to nanometer precision. Several experiments will be described and conducted in order to analyze the dynamics of the PET, and the results will be related to existing theory on the subject.

The mechanical setup and the experiments conducted for this thesis are heavily inspired by the groundbreaking efforts led by Andrew J Fleming and Reza Moheimani at the Laboratory for Dynamics and Control of Nanosystems, The University of Newcastle, Australia. The results of the experiments conducted will be related to their findings wherever comparison is feasible.

1.3 Structure of this document

In Chapter 2, the field of nanotechnology and especially nano scale microscopy will be reviewed as a background for this thesis. In Chapter 3 an experimental setup is presented, specifications of the equipment utilized are found and current theory on piezoelectricity is reviewed. In Chapter 4 several experiments are presented and performed on the PET in order to analyze its dynamical properties, and the results are presented. These results are then evaluated in the context of current literature on the subject. In Chapter 5 the results from earlier chapters are summarized, sources of error are presented, and conclusive remarks are presented.

Chapter 2

Background

2.1 Nanotechnology

Nanotechnology was first coined as a term by N. Taniguchi in 1974 as "the processing of, separation, consolidation, and deformation of materials by one atom or one molecule." But already in 1905, R. Zsigmondy published studies of particles down to $10\,nm$, using an ultramicroscope [1]. Today, nanotechnology is used to describe a vast number of fields, all involving the study of matter on an atomic scale. Some examples of nanometer size objects are shown in Table 2.1. Continuous progress in the areas of miniaturization and manufacturing has led an increasing number of scientific and commercial fields into the domain of nanotechnology, as has been the case with for instance the electrical transistor.

Diameter of Helium Atom	$0.032\,nm$
Diameter of Cesium Atom	$0.520\,nm$
Width of DNA Nucleotide	$0.330\,nm$
Width of DNA Chain	$2.2 - 2.6\,nm$
Diameter of Influenza Virus	$80 - 120\,nm$
Diameter of Human Red Blood Cell	$6000 - 8000\,nm$
Width of Human Hair	$> 18000\,nm$

Table 2.1: Some example entities of nanometer scale

2.2 Scanning Probe Microscopy

One of the distinguishing features of nanotechnology is that the sizes are smaller than the wavelength of visible light (about $400 - 700\,nm$) and so normal optical microscopes are rendered useless for imaging the objects. This has given rise to the area of nano microscopy, techniques for imaging objects down to atomic scale.

One of the branches of nano microscopy is that of scanning probe microscopes (SPMs). These microscopes enable researchers to form images of samples with reso-

lutions surpassing what is possible using optical techniques, by using a tiny probe to scan the sample and measuring the forces working on the probe. The maximum resolutions possible for different microscopes are shown in Table 2.2.

Common for SPM is that a nano size cantilever probe is held in proximity to the surface of the sample. Depending on the configuration, either the probe or the sample is moved in a raster scan so as to cover the entire area of the sample with the probe, and continuously record the forces working on the probe depending on its position.

There are several different types of SPM, with varying resolution, range and speed and with different uses. The most common types are discussed in this section.

Type	Resolution
Optical	$200\,\mathrm{nm}$
STM	$1\,\mathrm{nm}$
AFM	$0.5\,\mathrm{nm}$

Table 2.2: Maximum resolution for different microscopy techniques [2].

2.2.1 The Scanning Tunneling Microscope

The first type of SPM invented was the scanning tunneling microscope (STM) by Binnig et al. in 1982 [3]. The STM records information about the sample by using the concept of quantum tunneling. The tip of the cantilever is of a conducting material. When the distance between the conducting tip and a sample of either a metallic or semiconducting material is small enough (no more than $10\,\mathrm{nm}$, electrons can tunnel from the tip to the sample.

In the STM, two different modes are used. In constant height mode, the height of the cantilever is held constant as it is scanned over the sample. The voltage is also kept constant, and the resulting current is measured. In constant current mode, the height of the cantilever is adjusted to keep both the voltage and the current constant, and the vertical position of the cantilever is measured. In both modes, the measurements are used to provide a topological map of the sample at atomic precision [2].

2.2.2 The Atomic Force Microscope

Another important type of SPM is the atomic force microscope (AFM), invented in 1986 by Binnig et al. [4]. The AFM records the nanoscale forces between the cantilever tip and the sample surface by optically measuring the deflection of the probe. Depending on the setup, the AFM can be used to measure mechanical contact forces, Van der Waals forces, capillary forces, chemical bonding, electrostatic forces and magnetic forces.

The AFM produces a topological image of the sample by optically measuring the deflection of the cantilever as it moves across the surface. The most common way of measuring the deflection is to use a laser beam directed at the tip of the cantilever.
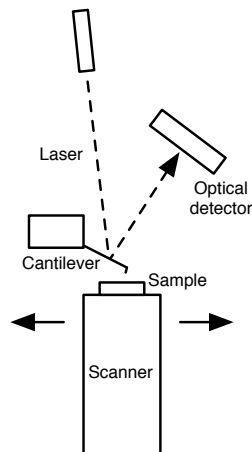
Figure 2.1: Common setup of AFM.

A common setup of the AFM is shown in Figure 2.1. The cantilever is held in place over the surface of the sample, while a scanner moves the sample in a raster pattern to measure the entire surface of the sample [2].

The movement of the cantilever is varying for different modes of the AFM. In static mode, also known as contact mode, the cantilever tip is brought into direct contact with the sample as the probe is scanned across the surface. This contact forces the tip to deflect, and this deflection is registered.

To minimize the effects of friction and to correctly measure soft surfaces, a tapping mode can be used. In this mode, the probe is oscillated as to constantly tap the surface of the sample, and the deflection is measured when the probe and the sample is in contact.
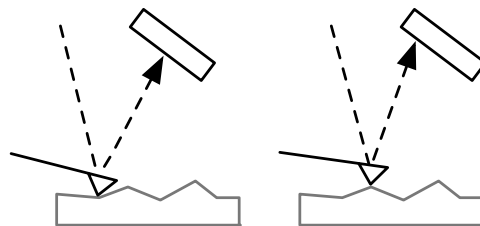

Figure 2.2: Contact mode operation of AFM.

In dynamic mode, also known as non-contact mode, the cantilever tip is oscillated in close proximity to the sample without touching it. In this mode, weak attractive forces such as van der Waals forces affect the probe and change the frequency of oscillation. This frequency change is then measured.

5

2.3 Piezoelectric Actuators

An important part of the SPM imaging setup is the scanner that moves the sample or cantilever around in order to measure the different areas of the sample. Piezoelectric actuators are by far the most commonly used to achieve this, and can be implemented in several ways. This section examines the most common techniques.

2.3.1 Piezoelectric Tripod Actuators

The first STM by Binnig et al. used a piezoelectric tripod as a scanner [3]. The piezoelectric tripod consists of three rods of piezoelectric material attached at the ends, as shown in Figure 2.3. The sample is then mounted on the intersection of the three rods.
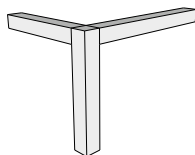

Figure 2.3: Mechanical setup of a piezoelectric tripod.

Piezoelectric materials have the property that they generate electric potential when being applied mechanical stress. This also works conversely; the materials produce stress and strain when an electric field is applied to them. When applying voltage to a rod, it contracts slightly, and the sample is deflected in the direction of the rod. This technique has not been in widespread use since the introduction of the piezoelectric tube actuator, which has similar characteristics using a more compact mechanical setup.

2.3.2 Piezoelectric Tube Actuators

Piezoelectric tube (PET) actuators are by far the most common actuators used in SPMs today [5]. The advantages of using piezoelectric tubes for actuation is that they can generate large forces with small amounts of power and within a reasonably compact design. Their simple design makes production relatively cheap, probably the main reason for their popularity. The drawbacks include a small displacement range and several disturbances and nonlinearities.

The PET actuator is made of a piezoelectric cylinder covered by conductive material on the inner and outer diameter. Most often this conductive layer is divided into several electrodes. By applying voltage to the various electrodes, displacements can be generated in three dimensions. Modeling of PET actuators is the focus of this paper, and will be described in greater detail in the following chapters.

2.3.3 Flexure Based Actuators

Flexure based actuators use piezoelectric stacks to actuate a platform connected to a base through several flexures. The sample is then mounted on this platform. Piezoelectric stacks consist of many piezoelectric elements joined together, resulting in a better voltage-to-displacement ratio than single piezoelectric slabs, but also causing more dominant nonlinear properties.

The setup of flexure based actuators is much more complicated than that of the tube actuator, resulting in significantly larger manufacturing costs. Because of this, their usage in commercial SPMs is rather limited. However, their improved properties – such as a larger range of motion and reduced cross coupling between axes – have recently generated increasing scientific interest and shown very good results, such as in [6].

Chapter 3

PET Actuator Setup

3.1   Introduction

This section will present the setup used throughout this thesis, where a PET is bent
in one direction by a high voltage signal on one of it's electrodes. The displacement of
the top of the PET will be measured simultaneously by both a capacitive sensor and
by a strain voltage sensor on the opposite electrode of the one actuating the PET. An
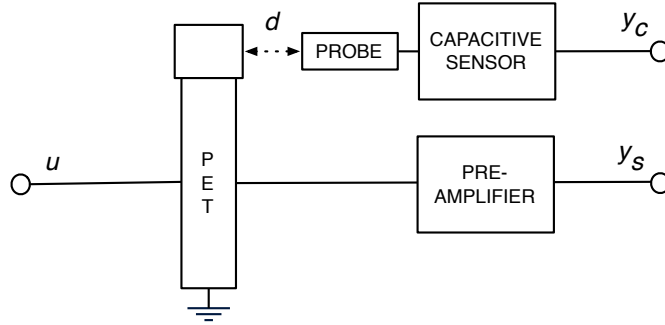illustration of this setup is shown in Figure 3.1.

Figure 3.1: Illustration of the basic experimental setup, showing the PET with its input
and outputs. u is the input voltage to the PET, d is the PET tip displacement, y_c is the
output voltage of the capacitive sensor and y_s is the output voltage of the strain voltage
sensor.

3.2 Piezoelectricity

Piezoelectricity is the ability of some materials to generate electric potential when applied mechanical stress. If not short-circuited, this potential induces a voltage differential over the material. This effect is called the direct piezoelectric effect. Piezoelectric materials are also deformed by applying a voltage field to them. This happens by the voltage polarizing the crystalline structures of the material, causing the crystals to alter their shape. This is called the transverse piezoelectric effect.

The piezoelectric effect is modeled by the piezoelectric constitutive equations, which can be written as

$$S_i = s_{ij}^E T_j + d_{mi} E_m \tag{3.1}$$

$$D_m = d_{mi} T_i + \epsilon_{mk}^T E_k \tag{3.2}$$

Here, s^E, d and ϵ^T are elastic, piezoelectric and dielectric constants of the material. The subscripts $i, j = 1, ..., 6$ represent the cartesian directions of the input and the reaction, respectively. S is the mechanical strain, T is the mechanical stress, D is the electrical displacement and E is the applied electric field. Thus, (3.1) is the transverse piezoelectric effect, while (3.2) is the direct effect. The transverse effect is illustrated in Figure 3.2.

The piezoelectric strain constant d deserves a more thorough review. This constant is given nominally for different piezoelectric materials, but has been shown to be significantly temperature dependent [7], and to change over time because of gradual depoling of the piezoelectric material. As such, any calculations relying on this constant are prone to deviations.
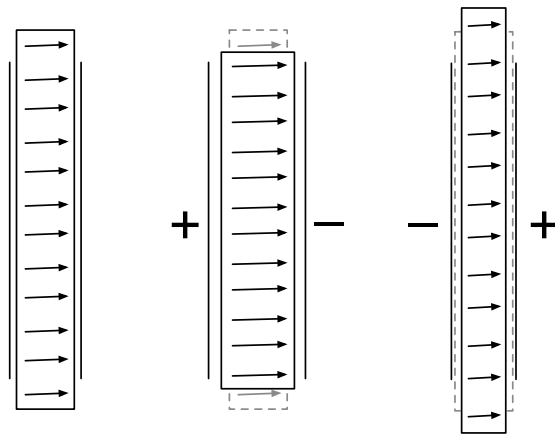
Figure 3.2: Illustration of the piezoelectric effect on a thin layer of piezoelectric material between a pair of electrodes. The poling n of the material is shown by the arrows. When voltage is applied in the same direction as the poling, the material expands along the poling axis, and thus contracts along the other axes. When voltage is applied in the opposite direction of the poling, the material contracts along the poling direction and expands along the other axes.

3.3 Mechanical Properties

PET actuators consist of a thin cylinder of radially poled piezoelectric material. The first piezoelectric tube actuator [8] was made of the ceramic lead zirconate titanate (PZT), and this material is still the most commonly used for tube actuators [9]. The piezoelectric tube is covered both on the inner and outer diameter by a layer of conducting material, commonly nickel, copper or gold, acting as electrodes for the piezoelectric material. Depending on the usage, these electrodes are most often divided into several sections, making it possible to apply a voltage differential across parts of the tube.

Figure 3.3: Photo of the PET.

The dimensions of piezoelectric tube actuators vary with the wanted scan range and precision. For larger displacements up to $100\,\mu\text{m}$, tubes of up to $80\,\text{mm}$ height are used due to their increased maximum range, while shorter tubes of $15\,\text{mm}$ are commonly used for smaller displacements of $15\,\mu\text{m}$ and lower since these generally have higher resonant frequencies and thus allow for higher scanning bandwidth [10].

The PET actuator used for this thesis was a piezoceramic tube of type PZT-5H manufactured by Boston PiezoOptics. It's made of lead zirconate titanate with the chemical composition $PbZr_{0.53}Ti_{0.47}O_3$, and has dimensions and properties listed in Table 3.1. A photo of it is shown in Figure 3.3.

As can be expected from a ceramic material, the PETs are very frail and should be handled with the greatest care so as not to induce cracks. Piezoelectric materials react to heat above what is called the Curie temperature. If the PET is heated above this temperature, which is given nominally for different types of piezo materials, all poling and subsequently all piezoelectric properties of the material disappear.

As shown in Figure 3.4, the PET is coated with electrodes of electronless nickel both

Property	Symbol	Value
Tube Length	L	$63.50\,\text{mm}$
Outer Diameter	D	$9.52\,\text{mm}$
Wall Thickness	h	$0.66\,\text{mm}$
Piezoelectric Strain Constant	d_{31}	$-265\,\text{pm/v}$
Relative Permittivity Constant	ϵ_{33}	3400
Curie Temperature		$195\,\text{oc}$

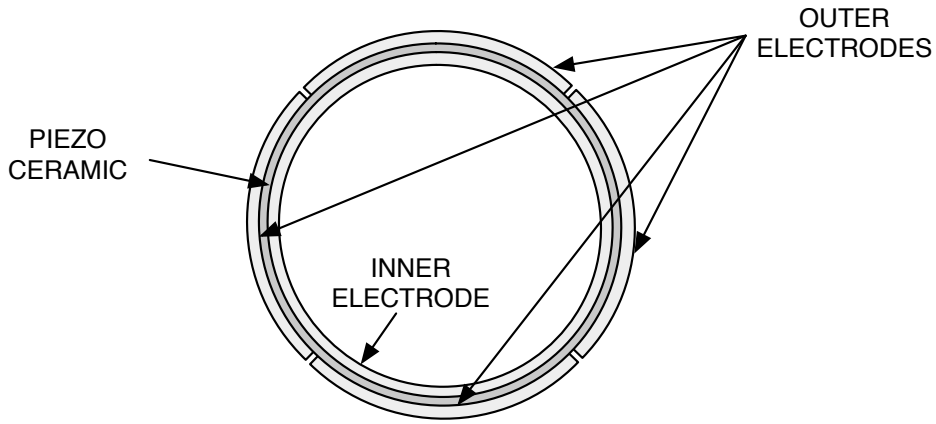Table 3.1: Properties of the PET chosen for this thesis

Figure 3.4: Illustration of the PET from the top. The thickness of the layers are exaggerated to show the details of the construction.

on the inner diameter and the outer. The inner electrode coating is circumferential, while the outer coating is partitioned into four electrodes. The electrodes can be attached to in- and outputs as shown in Figure 3.5. By applying voltage to the various electrodes, the PET can generate displacement in three dimensions.

The radial poling of the PET Movement in the z direction is either generated by applying voltage to all the external electrodes, causing the whole tube to expand/contract, or by applying voltage to the inner electrode. This movement can be modeled by

$$\Delta L = L(E \cdot n)d_{31} = \frac{LV}{h}d_{31} \tag{3.3}$$

where L is the length of the PET, E is the electrical field applied, n is the poling direction, V is the voltage applied and h is the wall thickness of the PET.
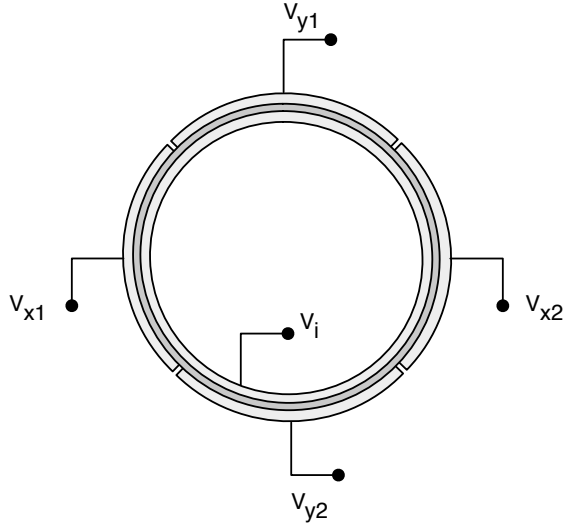
Figure 3.5: Illustration of the PET from the top, with the possible connections shown.

When a positive voltage field is applied to one of the quartered electrodes, the resulting contraction of the piezoelectric material will only take place for the quadrant of the tube covered by that electrode, while the other quadrants will try to maintain their shape. The elastic properties of the tube then forces the tube to bend towards the contracted quadrant. The opposite happens when a negative voltage field is applied - one quadrant will expand while the others will try to maintain the original shape, and the tube will bend away from the expanded quadrant.

Chen [11] used elastic methods to find an approximate linear expression for the displacement generated from applied voltage. Two voltages of opposing sign and amplitude V are applied on the x direction electrodes, while the y direction electrodes are grounded. This generates a strain in the z direction

$$S_3 = d_{31}V/h \tag{3.4}$$

where h is the thickness of the outer piezoelectric layer. This strain creates a stress on the tube in the z direction given by

$$\sigma_3 = Y S_3 \tag{3.5}$$

These forces create a torque causing the tube to bend sideways. This bending then generates an opposing torque, causing an equilibrium where the the total torque is zero. Chen assumes that the stress is linearly dependent on d, and finds the curvature of bending to be

$$R = \frac{\pi D h}{4\sqrt{2}d_{31}V} \tag{3.6}$$

14

From this, the analytical expression for the theoretical displacement $\bar{d}$ is found to be

$$\bar{d}_{double} = 2KV = \frac{2\sqrt{2}d_{31}L^2}{\pi Dh}V \tag{3.7}$$

This thesis only looked at actuation of the PET in the one direction. Because of the symmetry of the tube, the results should be identical for movement in the perpendicular direction as well. In order to both actuate the PET and measure the displacement at the same time, only $u = V_{x1}$ was connected to the input amplifier. The opposite external electrode $y_c = V_{x2}$ was connected to the output of the system in order to measure the piezoelectric strain voltage, while the internal electrode V_i was connected to ground.

When voltage is applied to only one electrode u, according to Chen the displacement is halved, giving the following expression for the theoretical displacement:

$$\bar{d} = Ku = \frac{\sqrt{2}d_{31}L^2}{\pi Dh}u \tag{3.8}$$

It should be noted that Chen's analytical solution uses the piezoelectric strain constant d_{31}, and is such exposed to factors mentioned earlier such as temperature dependency and gradual depoling.

Piezoelectric materials are also dielectric, so electrically, they behave like capacitors. Following the equation for capacitors, the capacitance across one of the electrodes is approximately

$$C = \epsilon_r \epsilon_0 \frac{A}{h} = \epsilon_r \cdot 8.854 \times 10^{-12} \frac{\pi D/4 * L}{h} = 21.6558 \, \text{nF} \tag{3.9}$$

where ϵ_r is the relative permittivity constant of the material, ϵ_0 is the permittivity of free space, D is the diameter of the tube, L is the length of the tube and h is the wall thickness.

3.4   High Voltage Amplifier

As discussed earlier, the applied voltage determines the magnitude of the displacement of the PET. As some samples can have a width of up to $100\,\mu\text{m}$, the range of the displacement should optimally be of the same scale. With the given specifications for the PET, the piezoelectric constant K becomes

$$K = \frac{\sqrt{2}d_{31}L^2}{\pi Dh} = -0.076556\,\mu\text{m/V} \qquad (3.10)$$

and so to accomplish a maximum displacement of $d_{max} = 50\,\mu\text{m}$ in any direction the input voltage u would need to be

$$u_{max} = \frac{d_{max}}{|K|} = 653\,\text{V} \qquad (3.11)$$

To amplify the input signals, a Trek Model PZD350 High Voltage Amplifier was used, shown in Figure 3.6. It has a maximum voltage of $\pm 350\,\text{V}$. While this is less than needed to generate the maximal $100\,\mu\text{m}$, it will be shown that it is enough to generate measurable displacements.

Slew rate is also something to be considered. A sine input with amplitude $A = 350\,\text{V}$ has a maximal slew rate of

$$slew = A2\pi f = 700\pi f\,\text{V/s} \qquad (3.12)$$

The Trek amplifier has a maximum slew rate of over $500\,\text{V/}\mu\text{s}$, giving that the maximal bandwidth available at maximal amplitude is

$$f = \frac{slew}{700\pi} = \frac{500 \cdot 10^6}{700\pi} = 227364\,\text{Hz} \qquad (3.13)$$

which is beyond the requirements for the experiments conducted for this thesis. The amplifier can deliver up to $40\,\text{kHz}$ with less than 1% distortion, enabling it to be treated as a linear gain for modeling purposes. It accepts input signals in the $\pm 10\,\text{V}$ range and has an adjustable gain. Before use, the amplifier was calibrated to generate a $^{10V}/_V$ gain by comparing the input and output voltage.

Since the PET electrically can be approximated by a capacitor, the impedance across one of the quadrants is given as

$$Z = \frac{1}{j\omega C} \qquad (3.14)$$

with j being the imaginary operator, ω being the AC frequency applied to the electrode, and C being the capacitance across a quadrant of the PET, found in the last section. A sine wave input of maximal voltage amplitude $350\,\text{V}$ and frequency $5000\,\text{Hz}$ would then result in a maximal current flow of

$$I_{max} = V_{max}2\pi fC = 238\,\text{mA} \qquad (3.15)$$

The amplifier is specified to deliver up to $400\,\text{mA}$ which should be exceedingly sufficient.

Figure 3.6: Photo of the Trek High Voltage Amplifier front.

3.5 Capacitive Sensor

In order to analyze the dynamics of the PET, precise measurement of the displacement generated from different inputs is needed. One of the most common equipment types used for measuring PET displacement today is the capacitive sensor [9].

Capacitive sensors are easy to implement and give a precise measurement. In general, the measurement is based on mounting a capacitive probe at a fixed point pointing towards an object of interest (the 'target'). For optimal performance this object has to have a flat surface facing the probe, and needs to be grounded to the capacitive sensor ground. The sensor can then measure the capacitive field between the probe and the target, and from this the distance between probe and target can be calculated.

Figure 3.7: Photos of the capacitive sensor a) gauge, b) probe and target.

For the experiments conducted for this thesis, the position of the top of the PET was measured capacitively by an ADE Technologies MicroSense II 6810 Gauging Module. The MicroSense sensor used an insulated probe of model MicroSense II 6501 with a diameter of 1 mm and a measurement range of $\pm 50\,\mu m$. The gauge is shown in Figure 3.7a and the probe mounted to face the target is shown in Figure 3.7b.

The output of the capacitive sensor was a voltage differential proportional to the measured displacement. The sensor was factory calibrated to guarantee an accuracy of ± 69.89 nm over the entire displacement range, up to a bandwidth of 100 kHz. The RMS noise level was given to be 0.204 mV.

An issue with this sensor is that the linear relationship between the displacement and the output voltage only holds when the probe surface and the target surface are aligned in perfect parallel. This makes careful directional targeting of the probe very important in order to achieve a precise result, which was ensured by using the rig described later in this chapter.

Also, positioning the probe to get the center position of the sensor to match the zero voltage displacement of the PET down to nanometer scale turned out to be exceedingly hard. This was accounted for by recording the measured position of the PET without any input signals applied, and then subtracting this value from the measurements recorded in subsequent experiments.

3.6   Piezoelectric Strain Voltage Sensor

Recent research led by AJ Fleming [10, 12, 13, 14] has shown that precise displacement measurements can be extracted from measuring the open-loop voltage induced on the opposite electrode of the one used for actuation. This measurement will be used to complement the capacitive sensor measurements in the experiments conducted for this thesis.
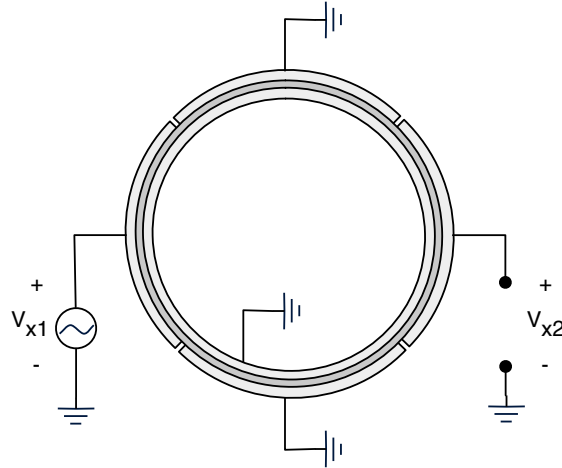

Figure 3.8: Top view of the PET, connected to measure strain voltage

When voltage is applied to one side of the PET V_{x1} while the inner electrode V_i is grounded, it forces that side to extend or contract depending on the polarity of the applied voltage. With no voltage applied to the opposite side, a contraction will force the tube to bend towards the side with applied voltage, while an extension will bend the tube the other way.

When the tube is bent, the direct piezoelectric effect causes a voltage linearly dependent of the displacement of the tube to be applied between the open electrode V_{x2} and ground. This voltage was measured as one of the outputs of the system. The setup is shown in Figure 3.8. According to Fleming et al.[10], it is possible to achieve tens of kilohertz bandwidth with as little as a few picometer noise amplitude using this measurement technique.

There are drawbacks to this method. One of the bigger issues is that the direct piezoelectric effect exploited for the measurement is just as dependent on the piezoelectric properties of the material as the transverse piezoelectric effect. This means that the measurement is dependent on temperature.

Also, because of the capacitive behavior of the PET, impedance at lower frequencies is extremely high. For this thesis work, the strain voltage output was fed through a SRS SR560 Low Noise Preamplifier, shown in Figure 3.10. Bhikkaji et al. [15] model a PET quadrant under stress as an ideal dependent voltage source in series with a capacitor

matching the capacitive properties of the material. The equivalent electrical circuit is shown in Figure 3.9 where y_s is the voltage measured by the SR560. The electrical equation is then

$$y_s = RI = RC\frac{d(V_p - y_s)}{dt} = RCj\omega(V_p - y_s) \tag{3.16}$$

The SR560 Preamplifier has an internal impedance of $R = 100\,\text{M}\Omega$, and with the PET capacitance $C = 21.6\,\text{nF}$ the transfer function from the internal strain voltage V_p to the measured y_s becomes

$$\frac{y_s}{V_p} = \frac{RCj\omega}{RCj\omega + 1} = \frac{j\omega}{j\omega + \frac{1}{RC}} = \frac{j\omega}{j\omega + 0.46} \tag{3.17}$$

This shows that the strain voltage measurement has a high-pass form with a cutoff frequency of $\frac{1}{2\pi RC} = 0.0737\,\text{Hz}$.
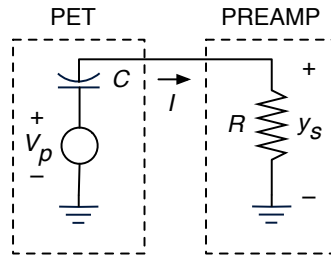
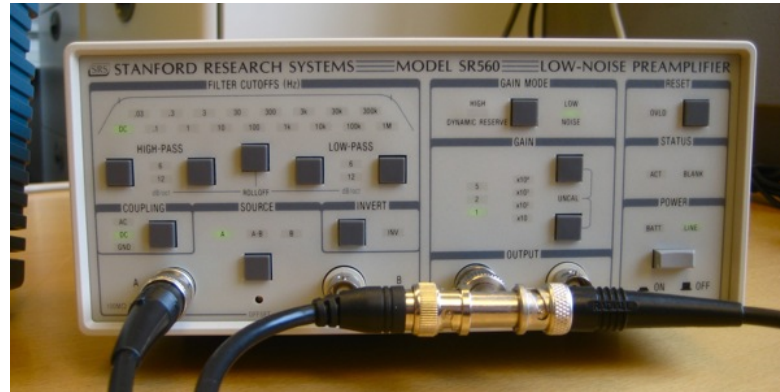Figure 3.9: Electrical circuit diagram for the strain voltage measurement.

Figure 3.10: Photo of the SRS SR560 Preamplifier.

3.7 Mounting and Fixtures

For precise measurements down to nanometer scale, any vibrations from the mechanical setup or the surroundings could have a severe impact on the result. Also, if not properly fixated, the vibrations of the PET could induce vibrations in the capacitive sensor. To minimize the input from the surroundings, a base and casing was constructed by the mechanical shop at the dept. of Engineering Cybernetics. The components along with measurements are shown in Figure 3.13, and in Figure 3.11 the components are shown assembled. Figure 3.12 shows photos of the PET mounted to the base.

(a) Top   (b) Side
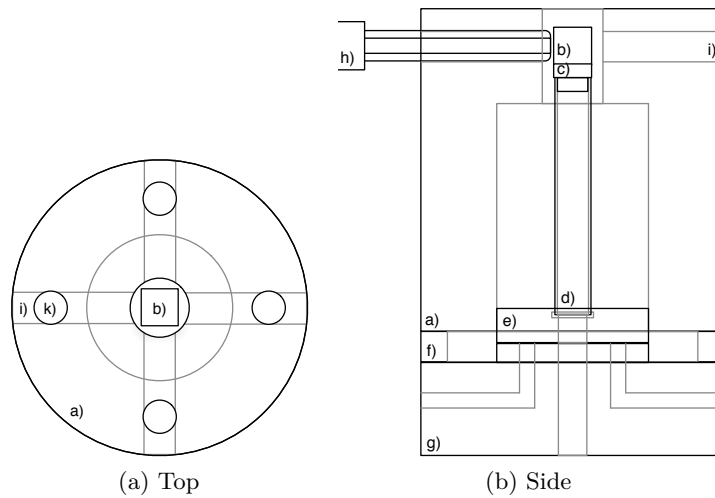
Figure 3.11: Schematics for mechanical setup

0.9 mm wires were soldered onto the PET outer electrodes, lead through the base to the outside and connected through BNC connectors to coaxial wires. Another wire was soldered onto the PET inner electrode and connected to the ground of the outer electrode BNC connectors.

The cylindrical base (g) was machined out of aluminum. The base has four threaded holes for attaching the casing using bolts, as well as four smaller threaded holes for attaching the insulating disc. Also, there are four L-shaped holes (i) connecting the outer sides through the insulating disc to the top of the disc. These are used to allow access to the wires soldered on to the outer PET electrodes from the outside of the casing. A hole in the center from top to bottom allows access to the inner PET electrode wire and the capacitive target wire from the outside.

The insulating disc (e) was made out of PVC to insulate the inner and outer electrodes from each other and from the base. The smaller hole matches the outside diameter of the PET, so that the PET fits tightly inside it. The larger diameter of the top of the hole was used to contain the glue fixing the PET to the insulating disc.

The PET (d) was fixed onto the insulating disc using a two component epoxy adhesive

21

with 12 hours of setting time. The PET was lodged just barely down into the inner hole of the insulating disc as shown in Figure 3.11b, and the glue was poured into the bigger top compartment. The casing was then assembled, and aluminum jigs were placed into the capacitive sensor holes and fastened in order to fix the capacitive target (b) into the centered position shown in Figure 3.11a.
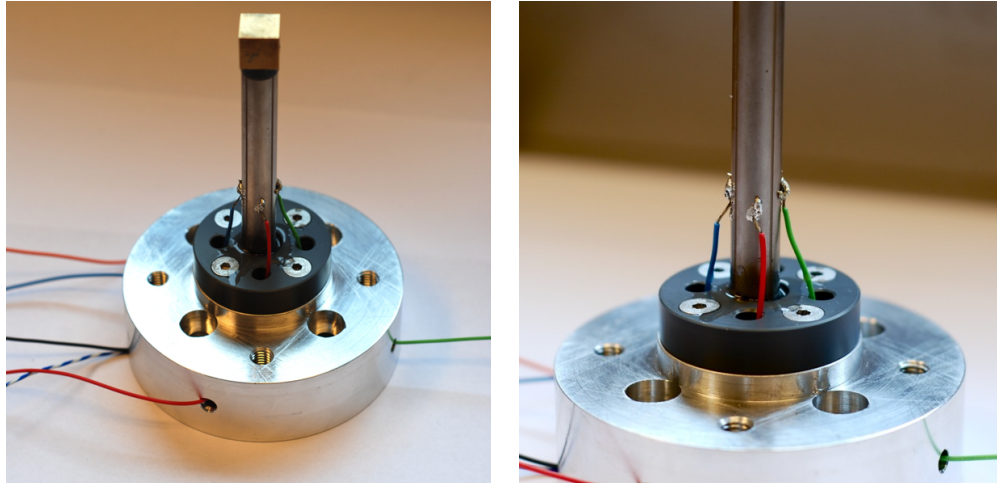

Figure 3.12: Photos of the PET fixed onto the insulating disc which is bolted to the base.

The capacitive target (b) was machined out of brass into a $1\,\text{cm}^3$ square cube weighing $9\,\text{g}$, with a small threaded hole through the bottom for attachment to the capacitive target base (c). A wire was soldered onto it, guided down the inside of the PET and grounded to the base and casing. The cylindrical capacitive target base was machined out of PVC to attach the capacitive target to the PET and to insulate it from the PET electrodes. The capacitive target base fits the inside of the PET tightly, and was lead down the inside of the PET to fix it.

The cylindrical casing (a) was machined out of aluminum to be fastened to the base, with a wide hole in the lower part and a smaller hole in the upper part. The casing was placed onto the adjustment cylinder (f) and fastened using screws to the base. Four holes were drilled from the side into the middle to allow the capacitive sensor probe (h) direct access to the capacitive target, shown in Figure 3.11b. Smaller threaded holes were drilled from the side of the casing into the side of the sensor holes, and PVC screws were placed into them to affix the capacitive sensors to the casing. The capacitive sensor probe was grounded to the base (and through that to the capacitive target) through its outer shell.

In order to minimize the effect of outside vibrations and noise, the base and casing was then placed on a wooden platform resting on a dampening layer of foam rubber. Photos of the complete setup is shown in Figure 3.14.
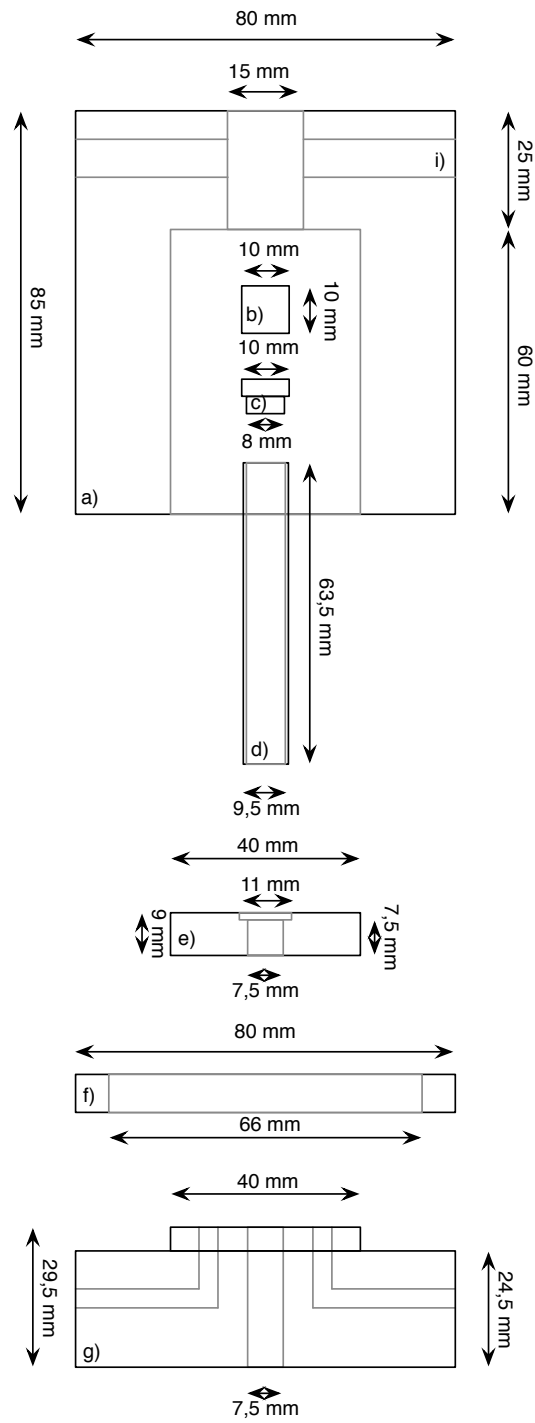
Figure 3.13: Measurements for the mechanical setup. The parts are named for reference in the text.
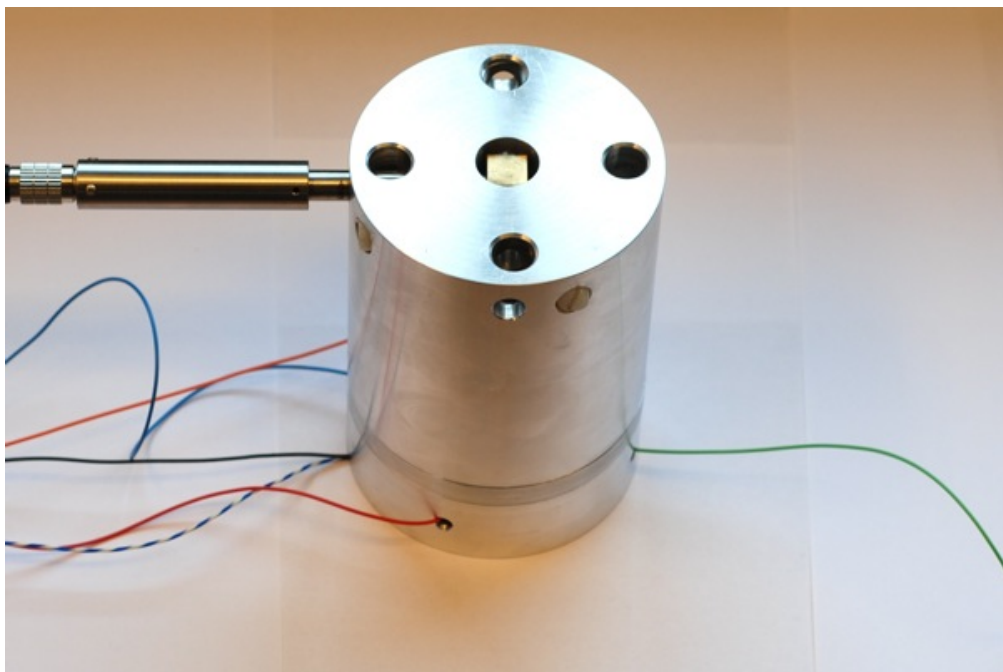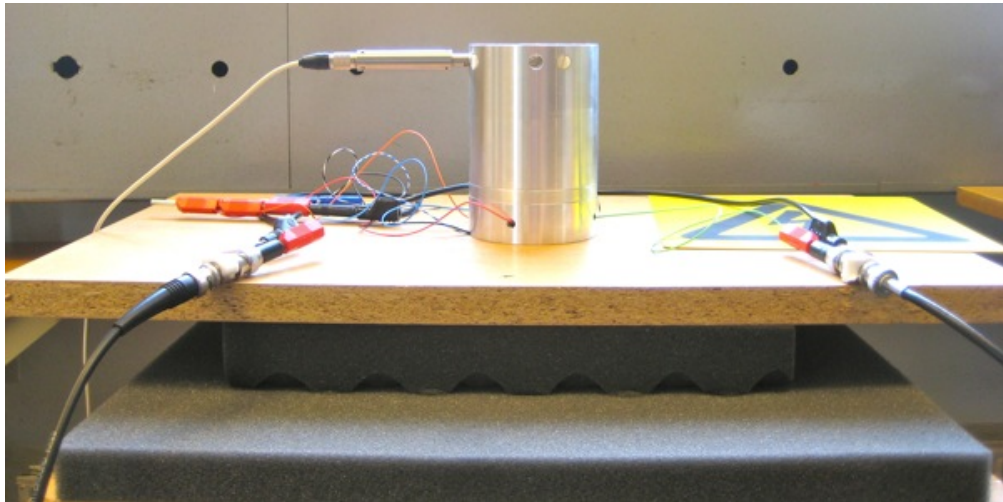
Figure 3.14: Photos of the mechanical jig assembled.

3.8   Signal Generation and Data Gathering

In order to actuate the system with the intended signals, the system was connected to a dSpace DS1103 Hardware-In-Loop (HIL) controller, shown in Figures 3.16a and 3.16b. The input of the system u was connected to one of the HIL controller's digital-analog (DA) channels through the high voltage amplifier, while the capacitive sensor and strain voltage output were connected to analog-digital channels of the HIL controller. The HIL controller was connected to an Intel PC running Windows Vista and Matlab R2008a through an optical connection and a dSpace DS819 PCI Express card.

Models for execution were designed in Simulink using standard blocks as well as input/output blocks provided by the dSpace HIL suite. The sample time of the system was set to 10^{-5}. The models were compiled and uploaded to the HIL controller using the application dSpace ControlDesk. This application was also used for monitoring the ADC channels of the HIL controller and downloading measurement data. This data was then imported into Matlab for further processing.

When sine wave signals were applied to the system, the output from the dSpace HIL was filtered through a SRS SIM965 Analog Filter (shown in Figure 3.16d) before being fed through the High Voltage Amplifier. The filter was setup as a low-pass Butterworth filter with cutoff frequency $6\,\text{kHz}$ and slope $12\,^{\text{dB}}/_{\text{oct}}$.. This was done to remove quantization noise generated by the HIL controller.

Frequency response data was recorded using a Solartron SI 1253A Frequency Response Analyzer (FR analyzer), shown in Figure 3.16c. The FR analyzer's generator output was connected through the high voltage amplifier to the system, Channel 1 of the FR analyzer was connected to the high voltage amplifier's voltage monitor output to record u and Channel 2 was connected to the measured output voltage, y_c or y_s depending on the experiment.
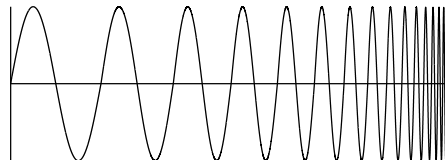
Figure 3.15: An illustration of swept sine waves.

The FR analyzer applied sine waves of increasing frequency to the system, as illustrated in Figure 3.15. For each frequency, the gain and phase differences between the input and output were recorded for a specified integration time interval. These values were then averaged. A longer integration time resulted thus in a smoother averaged gain and phase estimate.

The FR analyzer was connected to the PC using a GPIB-USB interface. The averaged data was transmitted to the PC using the application Frequency Response Analyzer by Solartron, and then exported to Matlab for plotting and further analysis.
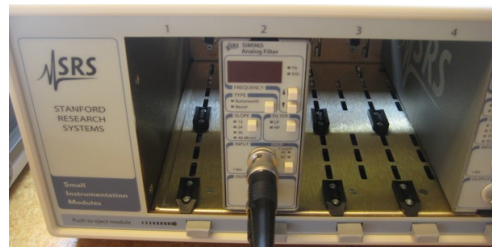
(a) dSpace HIL controller

(b) dSpace HIL Board

(c) Solartron FR analyzer

(d) SRS Scaling Amplifier

(e) Left side

(f) Right side

Figure 3.16: Photos of the setup.

Chapter 4

Experiments

This chapter will describe a series of experiments conducted on the PET actuator in order to analyze its properties. The results of these experiments will be presented, discussed and related to existing literature.
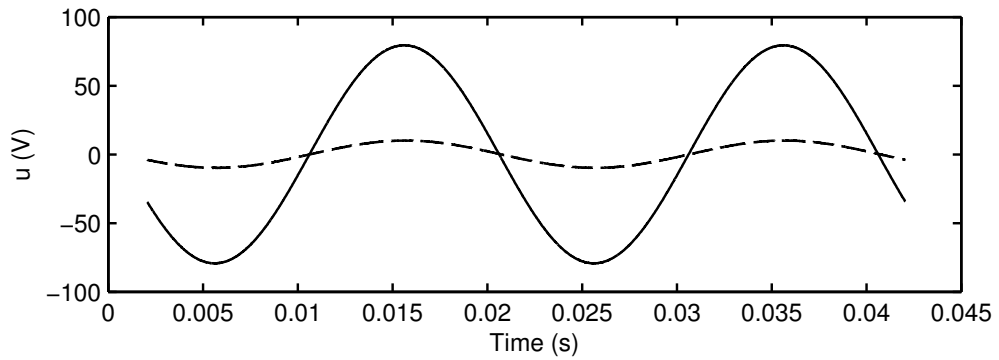
4.1   Sine Wave Response

Introduction

For a quick look at how the system reacts to sinusoidal input, the HIL controller was used to apply sine wave inputs of frequency $50\,\text{Hz}$ and amplitudes $10\,\text{V}$ and $80\,\text{V}$ to the input u.

Results

The input and output measurements are shown in Figure 4.1. The capacitive sensor voltage y_c follows the input voltage u closely with approximately the same frequency and phase, although with a much smaller amplitude. This is expected, as the amplitude of y_c is calibrated to proportionally match the measured displacement of the tube, not the input voltage. This will be discussed in the following sections. For the $80\,\text{V}$ input, the amplitude of y_c is approximately 1.47% of the amplitude of u. The strain voltage output y_s also follows the frequency and phase of the input u at this frequency. Again, the amplitude of the output is smaller than the input, by approximately 1.55%.
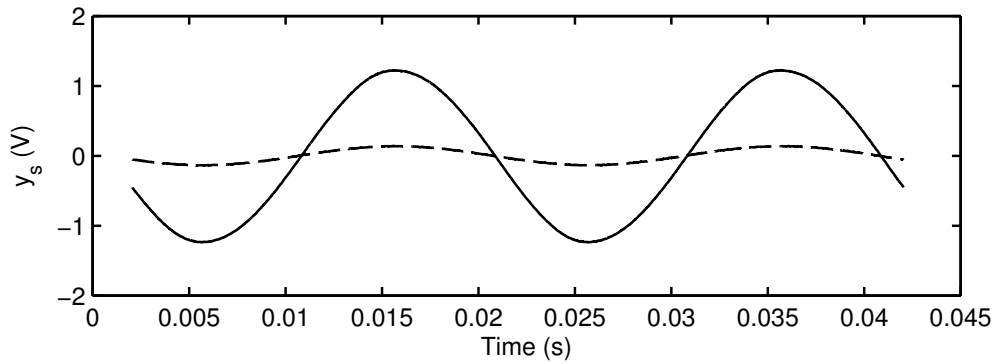
For both measurements, the signal-to-noise ratio seems to be very good, both when applying $80\,\text{V}$ and $10\,\text{V}$ input. This is further discussed in Section 4.7.

27
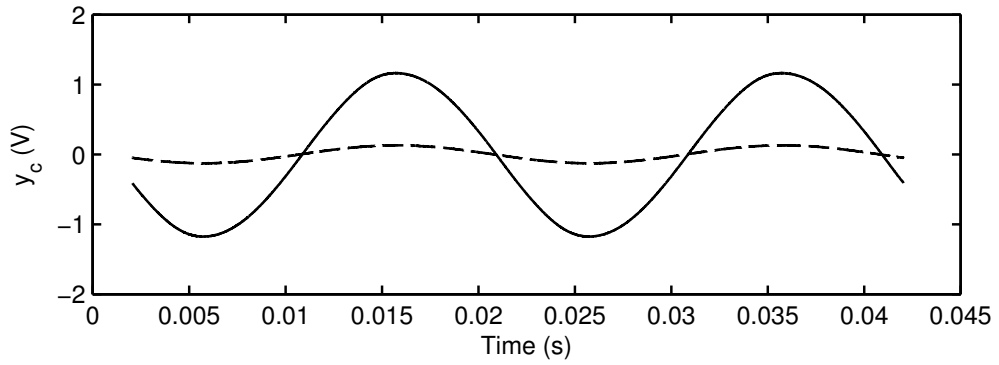
(a) Input voltage u

(b) Capacitive Sensor Output Voltage y_c

(c) Strain Voltage Output y_s

Figure 4.1: Plots of the system response to sine waves of frequency $50\,\text{Hz}$ to the PET. Solid line amplitude $80\,\text{V}$, dashed line amplitude $10\,\text{V}$.

4.2 Capacitance Measurements

Introduction

According to the specifications given and calculations performed in Section 3.3, the capacitance from each of the external electrodes to the internal electrode should be 21.6558 nF. In this experiment the actual capacitances of the electrode pairs was measured.

The capacitances were recorded by disconnecting all wires from the PET and using a Fluke 289 Multimeter connected directly to the inner electrode and each of the outer electrodes in turn.

For comparison the same measurements were done on two unused PETs of the same type as the one used in the setup. These PETs had not been subjected to soldering of any kind.

Results

Electrode	$x1$	$x2$	$x3$	$x4$	Average
Capacitance PET 1	14.3 nF	17.8 nF	19.1 nF	17.6 nF	17.20 nF
Capacitance PET 2	19.7 nF	20.7 nF	18.1 nF	19.7 nF	19.55 nF
Capacitance PET 3	21.0 nF	20.1 nF	19.1 nF	20.1 nF	20.08 nF

Table 4.1: Measured capacitance from outer electrodes (referenced as in Figure 3.5) to inner electrode. PET 1 is the PET in use, PET 2 and PET 3 are spare unused PETs.

The capacitances across the quadrants for the PET in use and two unused PETs are shown in Table 4.1. For all the tubes, the capacitances are lower than what the calculations would imply. This difference could be due to several factors. One factor is that the calculations used to find the the geometry of the tubes are not completely precise as all physical objects have imperfections. These imperfections could have a slight impact on the capacitance.

The lower capacitance could also mean that the piezo material has been slightly depoled. As discussed in Section 3.3, this can happen if the material has been exposed to heat over its Curie temperature, such as during soldering. PZT-5H has a relatively low Curie point compared to other piezo ceramics, according to the manufacturer it is 195 ∘c. For the two unused PETs depoling because of temperature should not be the case, as they have been kept unused at room temperature. But PET 1 has noticeably lower average capacitance compared to the unused ones, something that could be explained by this factor. Since each of the electrodes have been soldered on individually, this could also explain the large variance in capacitance for the electrodes. The $x1$ electrode has a significantly lower capacitance than the others, which again could be the result of partial depoling during the soldering of the electrode.

An eventual depoling of the material could have an impact on the results to be expected from the experiments detailed in this thesis. This will be discussed when it applies.

4.3 Frequency Response

Introduction

The PET actuator system has one input u and two outputs y_c and y_s, denoting the output voltages from the sensors. Assuming a linear relationship between the input and the two outputs, the relationships can be expressed as two linear transfer functions $G_c(s)$ and $G_s(s)$ with

$$G_c(s) = \frac{y_c}{u} \qquad G_s(s) = \frac{y_s}{u} \tag{4.1}$$

In this experiment, the frequency response of these transfer functions was plotted using the Solartron FR analyzer. The FR analyzer applied a series of sine inputs with a voltage of 80V for 200 frequency points from 1 Hz to 1200 Hz to the system. The resulting output signals were recorded, and the gain and phase differences were calculated and averaged over 2 seconds for each frequency point.

Results

The recorded frequency response of $G_c(s)$ is shown in Figure 4.2. For low frequencies, the gain is around -40.1 dB, with a phase of -1.5 degrees. There is a resonant peak at 332.4 Hz with a gain of -15.45 dB.

The frequency response of $G_s(s)$ is shown in Figure 4.3. For low frequencies, the gain is -39.6 dB, with a phase of -1.5 degrees. There is a resonant peak at 332.4 Hz with a gain of -11.37 dB.

The close resemblance between the two measurements confirms that the strain voltage sensor is representative of the displacement of the tube. The dynamics are closely related, with almost the same low frequency gain and a resonance peak at the same frequency. The gain around the peak is higher for the strain voltage measurement, and at frequencies above the peak the capacitive measurement has a slightly steeper slope than the strain voltage.

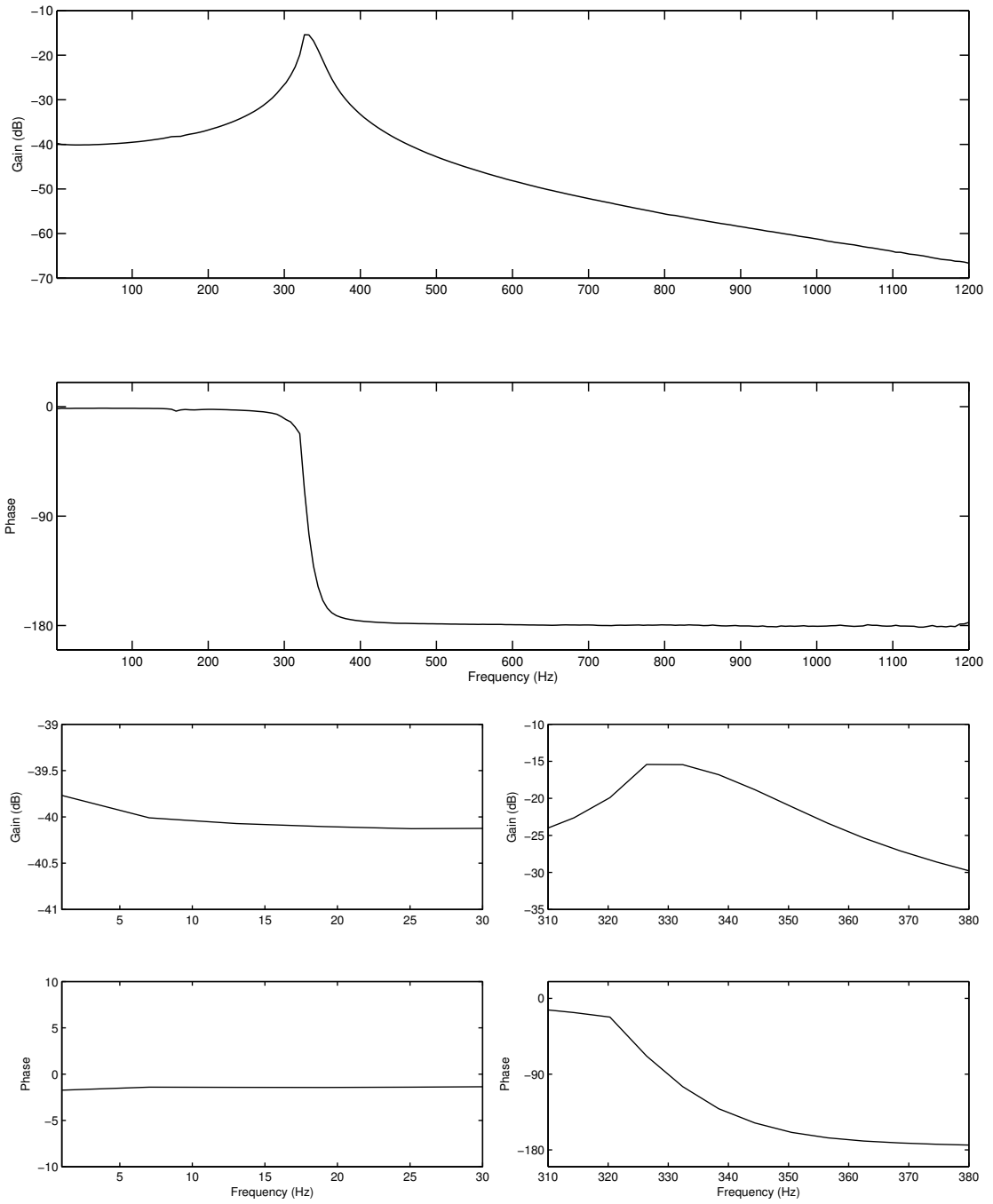These results are further discussed in the next sections.

Figure 4.2: Plot of the recorded frequency response of the transfer function $G_c(s)$ from the input voltage u to the capacitive sensor voltage y_c, measured by the FR analyzer in 200 points from 1 Hz to 1200 Hz. The lower graphs are of the same plot as the upper, only scaled up to showcase the difference at the lowest frequencies and around the peak.
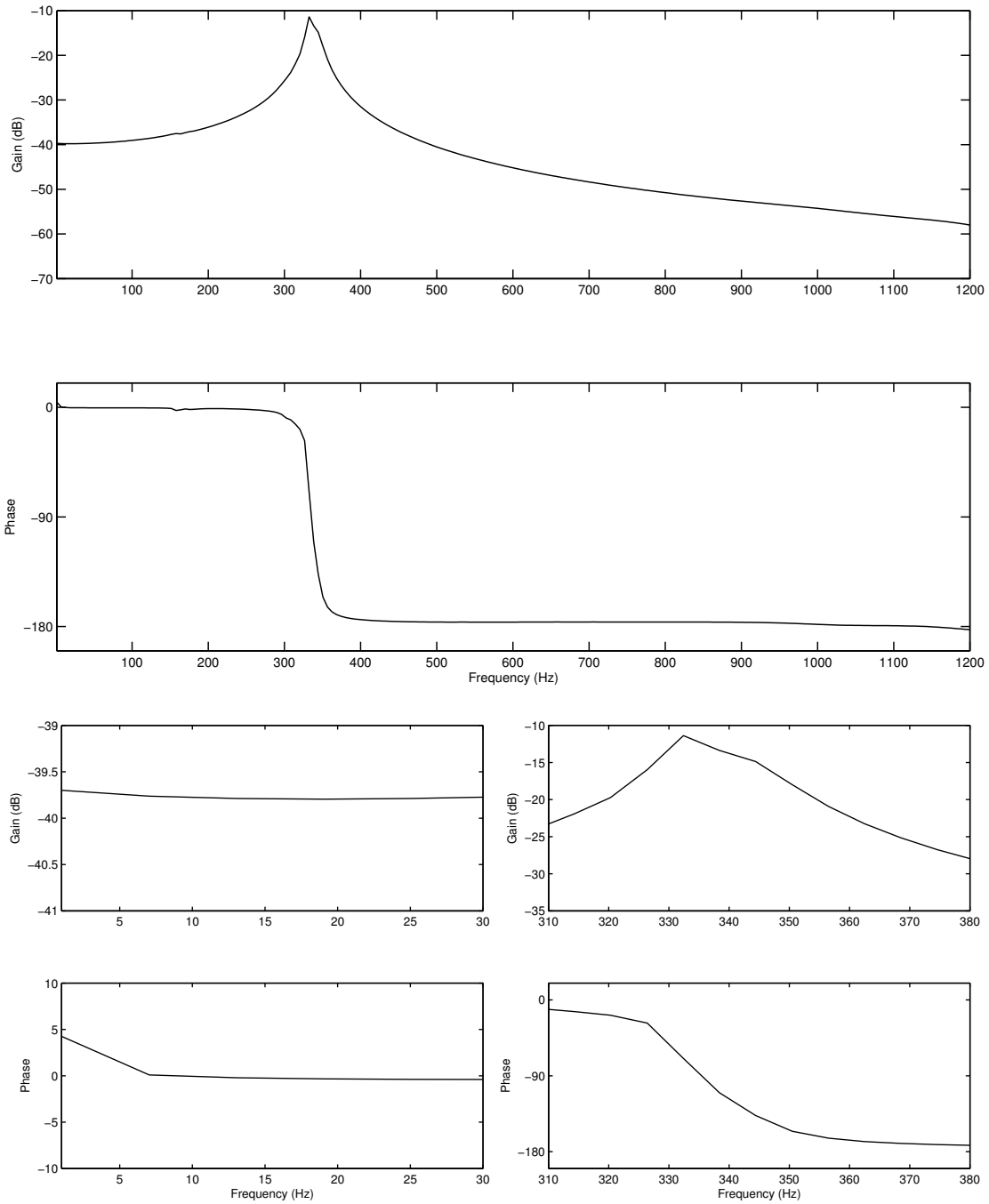
32

Figure 4.3: Plot of the recorded frequency response of the transfer function $G_s(s)$ from the input voltage u to the piezoelectric strain voltage y_s, measured by the FR analyzer in 200 points from 1 Hz to 1200 Hz.

4.4 Displacement

Introduction

So far the PET dynamics have been modeled by the relationship between applied voltage and the output voltage of the sensors. By applying a few assumptions about the internal dynamics of the PET and of the sensors, the tube can be analyzed further. It is known that the applied voltage u results in a displacement d, which is measured by the two sensors and thus through the sensor dynamics is turned into the output voltages y_c and y_s. It can be assumed that any measurement noise is added onto the actual displacement d to form the measured displacements d_c and d_s. The internal model of the piezotube is then given as

$$y_c = S_c(s)d_c = S_c(s)(d + n_c) = S_c(s)(P(s)u + n_c) \tag{4.2}$$

$$y_s = S_s(s)d_s = S_s(s)(d + n_s) = S_s(s)(P(s)u + n_s) \tag{4.3}$$

where $S_c(s)$ and $S_c(s)$ are the internal dynamics of the two sensors, and n_c and n_s represent the measurement noise of the sensors. This is shown in Figure 4.4. In order to find the relationship between applied voltage and the measured displacements d_c and d_s, the sensor dynamics was modeled and inverted.
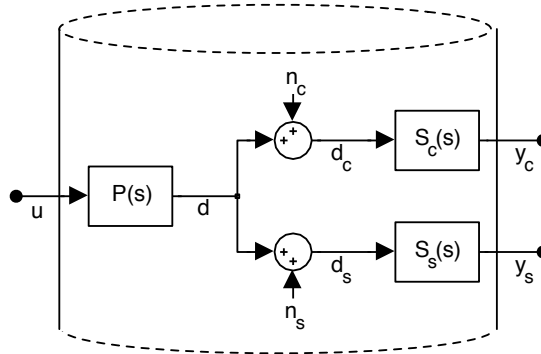

Figure 4.4: Block diagram of the PET dynamics.

The capacitive sensor specifications guarantee that the relationship between the measured displacement and the output voltage is within $\pm 0.07\%$ of linear. For simplicity it was therefore assumed that the capacitive sensor dynamics were constant, with the scaling factor being

$$S_c = \frac{y_c}{d_c} = \frac{10\,\text{V}}{50\,\text{μm}} = 0.2\,\text{V/μm} \tag{4.4}$$

and so the inverted dynamics of the capacitive sensor can be found as

$$S_c^{-1} = \frac{1}{S_c} = 5\,\text{μm/V} \tag{4.5}$$

The frequency responses for $G_c(s)$ and $G_s(s)$ displayed in Figures 4.2 and 4.3 show that the dynamics of the two sensors are very similar. From this fact it was assumed that the relationship between the PET displacement and the strain voltage output was also linear, and could be expressed as a scaling factor.
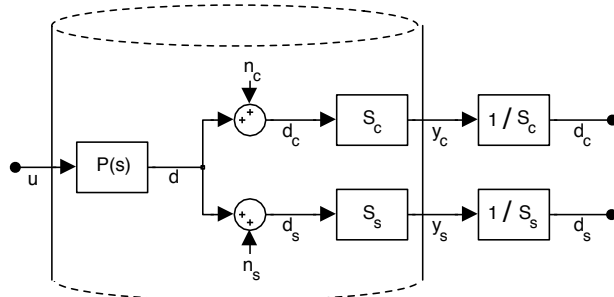

Figure 4.5: Block diagram of the PET dynamics with inverted sensor dynamics.

To find the strain voltage scaling factor S_s, the capacitive sensor measurement was used as reference, and a $50\,\mathrm{Hz}$ sine wave with amplitude $80\,\mathrm{V}$ was applied on u. By disregarding the noise and thus assuming that $d_c = d_s = d$ at this frequency, and by comparing the measured voltage outputs, the scaling factor for the strain voltage sensor was found to be

$$S_s = \frac{y_s}{d_s} = \frac{y_s}{d_c} = \frac{y_s}{S_c^{-1}y_c} = \frac{y_s}{y_c}S_c = 0.21\,\mathrm{V/\mu m} \tag{4.6}$$

and the inverted dynamics

$$S_s^{-1} = \frac{1}{S_s} = 4.761\,\mathrm{\mu m/V} \tag{4.7}$$

The estimated relationships between applied voltage u and the measured displacements d_c and d_s can be expressed as

$$d_c = S_c^{-1}S_c(P(s)u + n_c) = P(s)u + n_c \tag{4.8}$$
$$d_s = S_c^{-1}S_c(P(s)u + n_c) = P(s)u + n_c \tag{4.9}$$

$$P_c(s) = \frac{d_c}{u} \qquad P_s(s) = \frac{d_s}{u} \tag{4.10}$$

In the case of perfect measurements with no noise, this becomes

$$P_c(s) = P_s(s) = P(s) \tag{4.11}$$

The PET system including inverted dynamics is shown in Figure 4.5. The frequency responses and sine responses from Section 4.1 were scaled by S_c and S_s to show the estimated PET dynamics $P_c(s)$ and $P_s(s)$. Also, by applying Chen's methods a theoretical displacement $\bar{d} = Ku$ was found and compared to the measurements. Then the frequency responses from Section 4.3 were scaled and plotted.

35

Results

The PET displacement measurements matching a sine wave input of 50 Hz is shown in Figure 4.6. It can be seen that at this frequency the scaled output signals d_c and d_s are a close match to the calculated theoretical displacement $\bar{d}$.

Figure 4.7 shows the frequency response of the two displacement measurements. The two measurements closely match each other at lower frequencies and around the resonant peak, but at higher frequencies the capacitive measurement shows a steeper descent than the strain voltage.

The amplitude gain at lower frequencies is approximately -146 dB, or 0.05 µm/v. Compared to the gain 0.076556 µm/v from Chen's equations, this is a reasonable result. The slightly lower gain than was expected could be due to depoling as mentioned in Section 4.2. The $x1$ electrode was the one used to apply voltage to the PET, and with the decreased capacitance suggesting a substantial depoling of the quadrant, this could affect the outcome significantly.

The resonant peak has a maximal amplitude of -121 dB for the capacitive sensor, and -118 dB for the strain voltage measurement. The lower peak for the capacitive sensor, along with the steeper descent after the peak could indicate a slight low pass behavior in the capacitive measurement compared to the strain voltage.

Resonant Frequency

Both measurements show the resonant peak at 332.4 Hz. Several scientific papers [16, 12, 10] have found this resonant peak to occur around $800-1200$ Hz for PETs of comparable dimensions. There are a few factors that could cause this admittedly major disparity. First, the PETs used in this experiment and the compared literature are of similar but not exactly equal dimensions. For instance, the PET in the Fleming et al. setup has smaller electrodes compared to the tube length than the setup used here. This could account for minor differences in dynamics but probably not such significant disparities as is found in this experiment. Secondly, the possible depoling of the piezoelectric material in the PET. Although this could cause significant changes in behavior, it is not likely that a mechanical property such as the harmonics of the tube would be significantly affected by it.

Thirdly and most importantly, the capacitive target used for this experiment is a solid brass cube of $1 \, \text{cm}^3$ which combined with the PVC mounting has a total weight of 9 g. Some of the compared results have been found using a hollow aluminum cube of 1.5 g as a target [10], while others have used methods of modeling that didn't require a mounted target at all [16]. An added weight mounted on the free end of the PET would most probably lead to a lower harmonic frequency such as the one seen in this experiment. The findings of Fleming et al. support this, as they find the frequency of the resonant peak significantly lowered just by adding a load of 1.5 g to the free end of their tube.
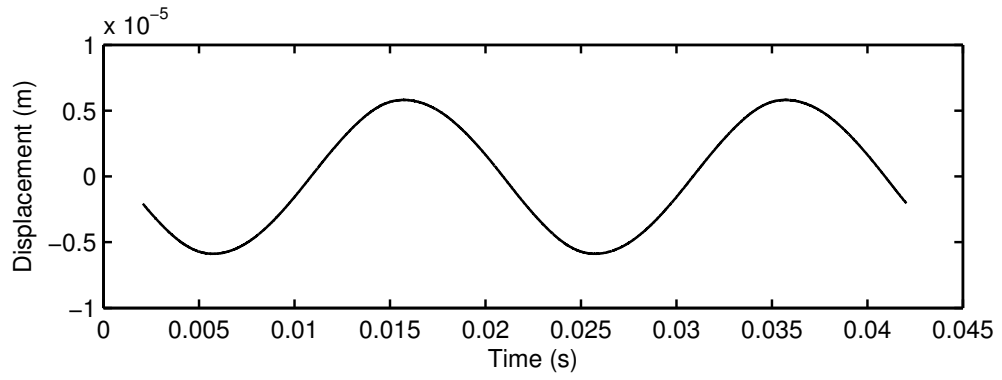
Strain Voltage Sensor Scaling

The scaling factor S_s from measured displacement to generated strain voltage was in this experiment found to be 0.21 V/μm. Fleming et al.[10] found this factor to be 6.2 V/μm, and Bhikkaji et al.[15] found it to be 4.955 V/μm. Both these values are an order of magnitude larger than what was found in this experiment. There are some differences in measurement technique that could account for this. While this experiment uses the SR50 Pre-Amplifier connected to the open-loop PET electrode, Fleming et al. use a home made low current-noise buffer stage to do the measurements. Bhikkaji et al. do not describe their measurement methods. While this does not give an answer to why the scaling factor is so much lower, different measurement techniques could very well lead to different measurements.

Another possible explanation for the different scaling factor is again the depoling mentioned in Section 4.2. The capacitance across the $x2$ electrode was found to be 17.8 nF, suggesting a depoling of parts of the electrode. It can be assumed that this depoling would lead to a lower conversion ratio between applied strain and generated voltage.
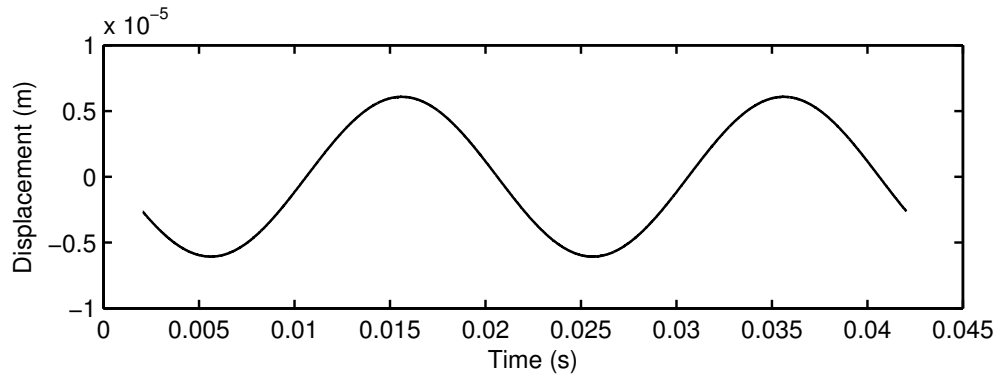
(a) Theoretical displacement from input signal $\bar{d}$

(b) Displacement measured by capacitive sensor d_c
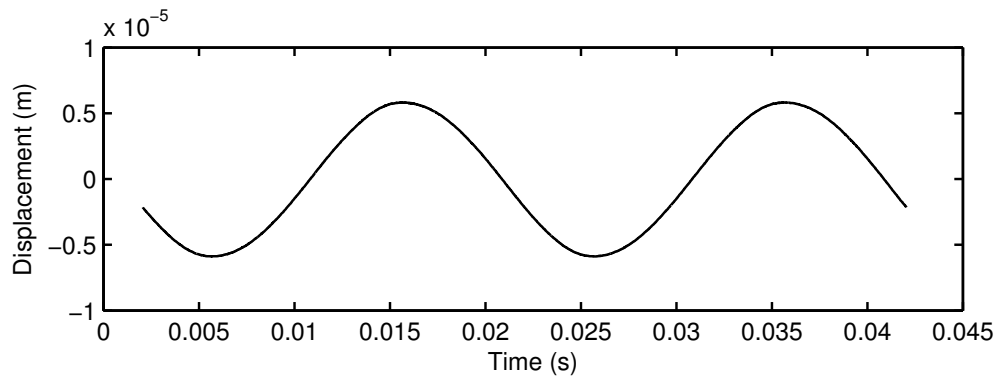
(c) Displacement measured by strain voltage d_s

Figure 4.6: Results from applying a sine wave of amplitude 80 V and frequency 50 Hz to the PET. Results are scaled to show the displacement calculated from voltage measurements.
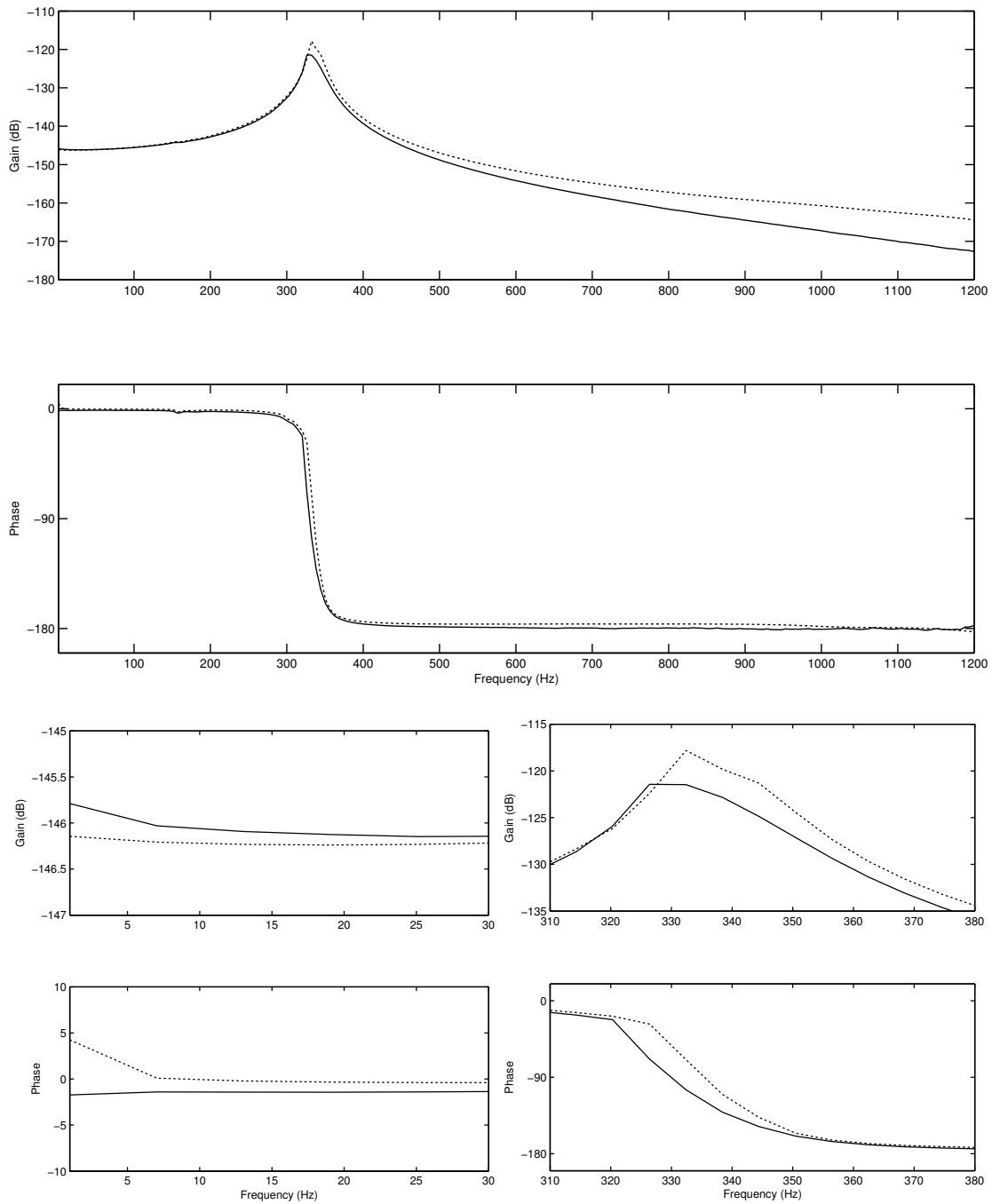
Figure 4.7: Frequency response data of the transfer functions $P_c(s)$ (solid line) and $P_c(s)$ (dotted) from the input voltage u to the piezoelectric strain voltage y_s, measured by the FR analyzer at 200 frequency points from 1 Hz to 1200 Hz.

4.5 System Identification

Introduction

A straightforward way of finding the dynamics of a PET system is by using system identification [12, 17].

System identification is based on modeling the dynamics of a system as a transfer function, by relating the inputs of the system to the outputs. The aim is to find a system model fitting as well as possible to the measurement data.

It was assumed that the systems could be expressed as linear transfer functions. An ARX form was used for the models to be estimated, with the general structure

$$y(t) + a_1 y(t-1) + \ldots + a_{n_a} y(t-n_a) = b_1 u(t-1) + \ldots + b_{n_b} u(t-n_b+1) + e(t) \quad (4.12)$$

or in the frequency domain

$$y(t) = \frac{B(s)}{A(s)} u(t) + \frac{1}{A(s)} e(t) \quad (4.13)$$

where $B(s)$ and $A(s)$ are polynomials of s with order and coefficients to be determined [18]. Both $G_c(s)$ and $G_s(s)$ have phase drops of 180 degrees, so it was assumed that $A(s)$ was of order 2. The order of $B(s)$ was assumed to be 3 to account for what looks to be a flattening of the downward slope at the high end of the frequency spectrum, giving models of the form

$$y(t) = \frac{c_1 s^2 + c_2 s + c_3}{s^2 + 2\zeta\omega_0 s + \omega_0^2} \quad (4.14)$$

where ω_c is the natural frequency and ζ the damping factor of the second order system.

In order to find the transfer functions of the system, the frequency transfer data was processed in Matlab using the functions from the System Identification Toolbox. The frequency response data was used to construct an idfrd object, which was input into the arx command along with the chosen model order.

The frequency responses of the resulting estimated transfer functions were then plotted against the measured data.

Results

The transfer function of $G_c(s)$ was found to be

$$G_c(s) = \frac{3.035 \times 10^{-4} s^2 - 0.1479 s + 4.239 \times 10^4}{s^2 + 91.76 s + 4.365 \times 10^6} \quad (4.15)$$

which divided by the scaling factor S_c gives the transfer function for $P_c(s)$ as

$$P_c(s) = \frac{1.518 \times 10^{-9} s^2 - 7.393 \times 10^{-7} s + 0.212}{s^2 + 91.76 s + 4.365 \times 10^6} \quad (4.16)$$

The natural frequency and damping factor of $P_c(s)$ is then

$$\omega_0 = \sqrt{4.365 \times 10^6} = 2089.258\,\text{rad/s} = 332.516\,\text{Hz} \qquad (4.17)$$

$$\zeta = \frac{91.76}{2 \cdot 2089.258} = 0.022 \qquad (4.18)$$

The natural frequency of the model is in accordance with what the frequency response plot of $P_c(s)$ suggests. A damping factor of 0.022 implies a significantly underdamped system, which also fits well with the resonant peak found in the measured frequency response. The frequency response of the model along with the measured response plot is seen in Figure 4.8. The model is seen to be following the measured response closely, with minor phase and gain differences in the low frequency domain. Around the resonant peak the model has a somewhat larger gain than the data.

The estimated transfer function of the relationship between applied voltage and strain voltage output $G_s(s)$ was found to be

$$G_s(s) = \frac{-4.822 \times 10^{-4}s^2 + 0.2051s + 4.638 \times 10^4}{s^2 + 80.09s + 4.463 \times 10^6} \qquad (4.19)$$

and thus $P_s(s)$ was given as

$$P_s(s) = \frac{-2.296 \times 10^{-9}s^2 + 9.766 \times 10^{-7} + 0.2209}{s^2 + 80.09s + 4.463 \times 10^6} \qquad (4.20)$$

with natural frequency and damping factor

$$\omega_0 = \sqrt{4.463 \times 10^6} = 2112.581\,\text{rad/s} = 336.228\,\text{Hz} \qquad (4.21)$$

$$\zeta = \frac{80.09}{2 \cdot 2112.581} = 0.019 \qquad (4.22)$$

This also looks to match the measured frequency response data reasonably well, with a resonant peak close to the resonant peak of $P_c(s)$, and an underdamping of the response. The frequency response of the model along with the measured response plot is seen in Figure 4.9. Again, the model seems to be a good fit for the data. The model does not account for the phase difference at the lowest frequencies, but both the resonance peak and the high frequency asymptote is followed closely.
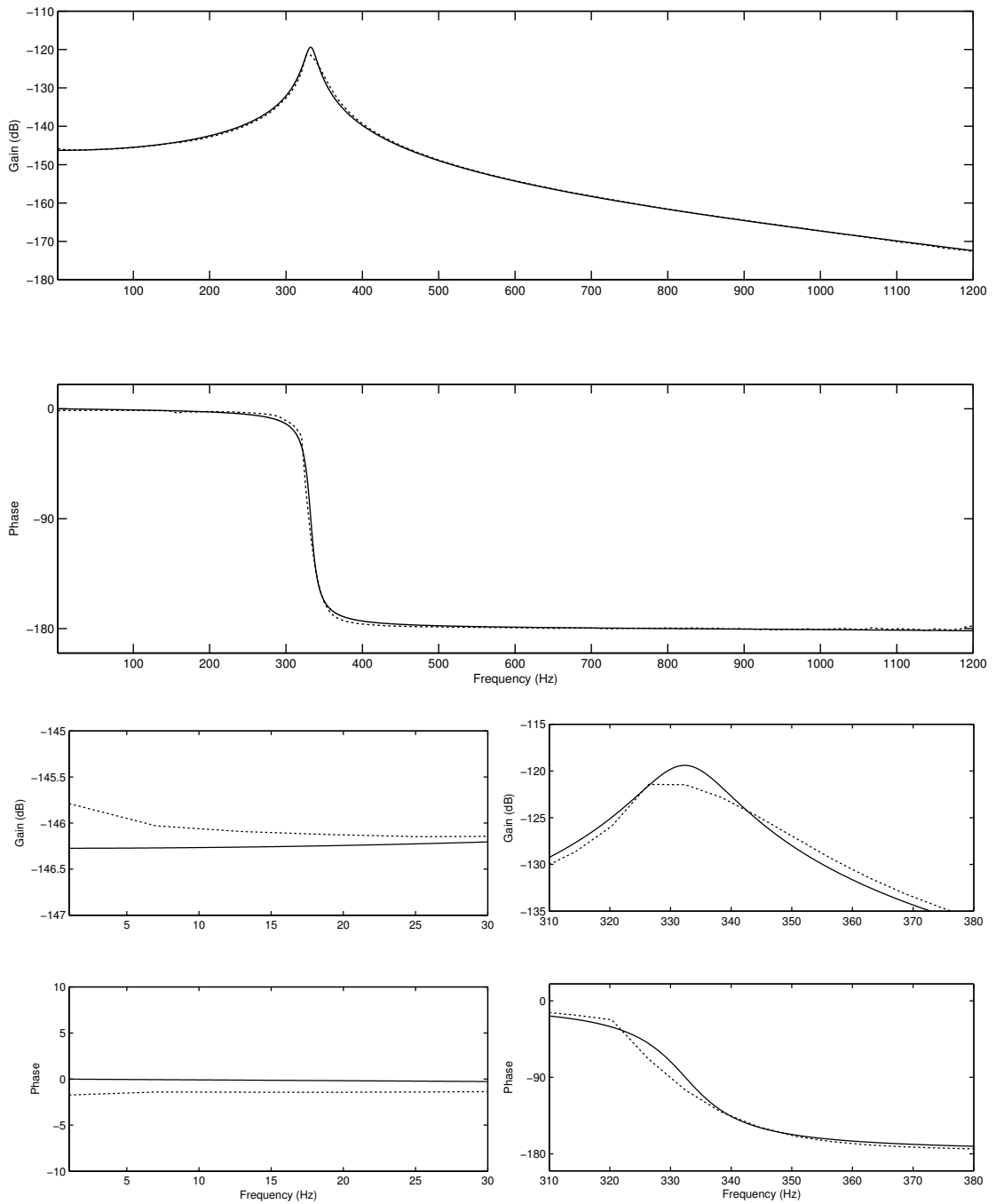
Figure 4.8: Frequency response data (dotted) and the identified transfer function (solid line) for $P_c(s)$.
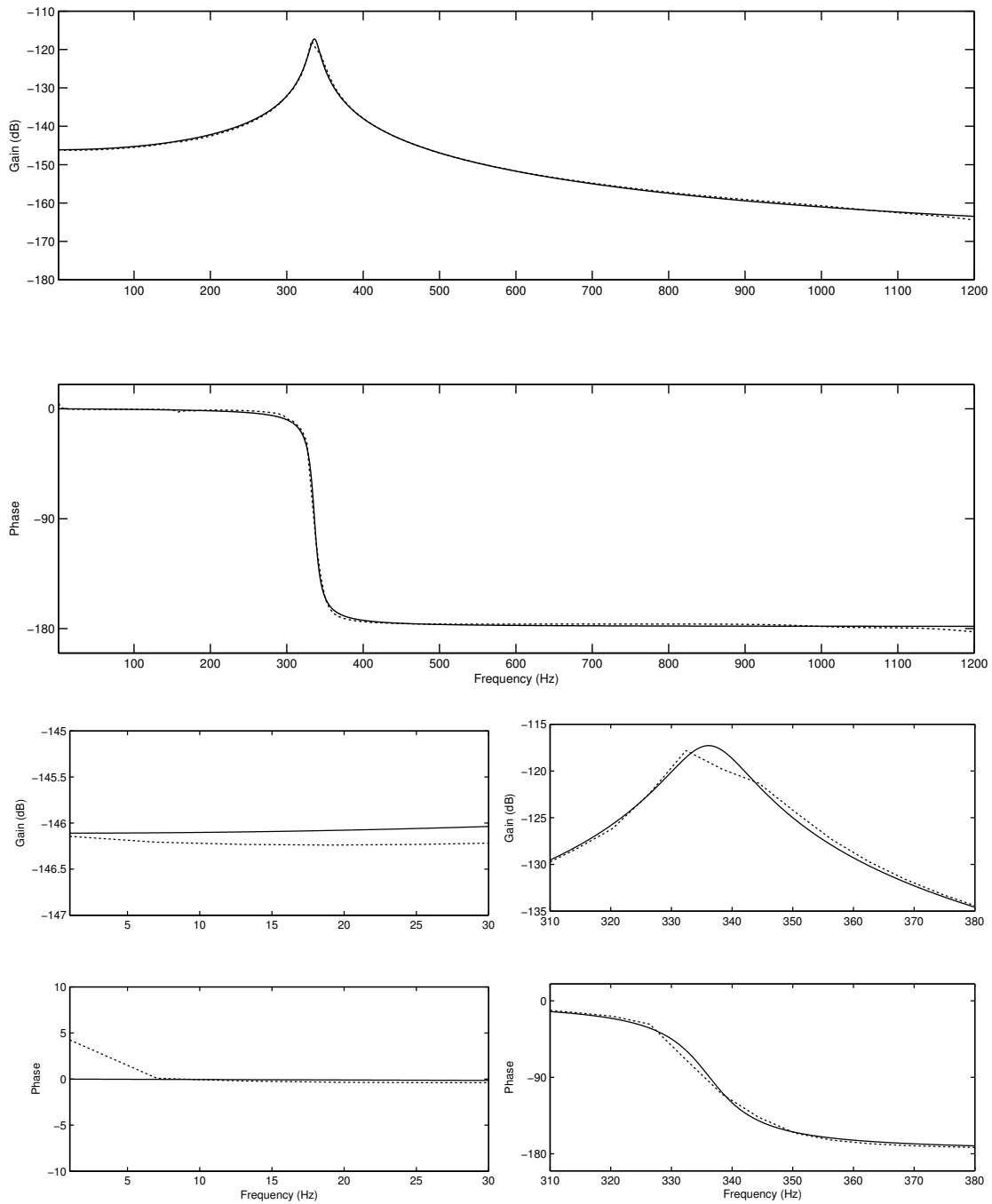
42

Figure 4.9: Frequency response data (dotted) and the identified transfer function (solid line) for $P_s(s)$.

4.6 Triangular Signal Response

Introduction

SPMs work by scanning the sample in a pattern so that the entire surface is measured. The most common way to scan a sample is to have a fast scan direction x, where a triangular scan pattern is applied, as shown in Figure 4.10. In the other lateral direction y, a slower step-ramp function is used. This movement is shown in Figure 4.11a. This causes the probe to scan one line in the x direction while keeping a steady set point in y, then return to the starting position of x while advancing one point in y.
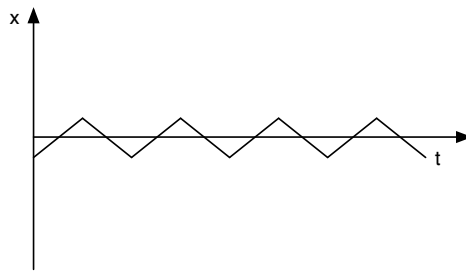

Figure 4.10: Illustration of scanning pattern, fast scan direction.

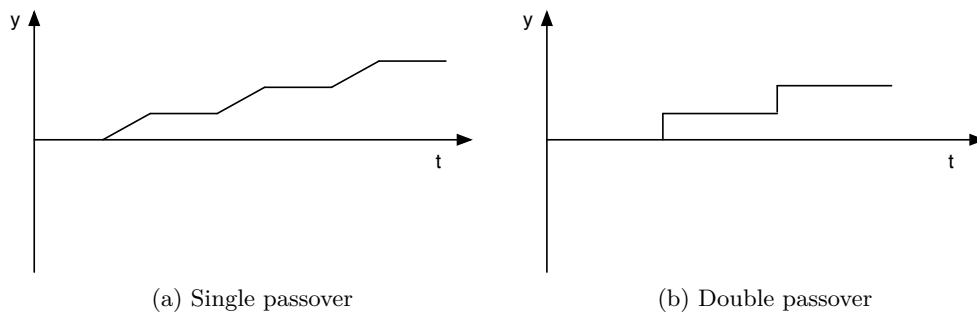(a) Single passover   (b) Double passover

Figure 4.11: Illustration of scanning patterns, slow scan direction.

Another common scanning pattern is using the same x movement, but replacing the y movement with a slower step y function as shown in Figure 4.11b. This causes the probe to scan a line in the x direction back and forth before skipping on to the next point in the y direction. This double passover is often used as a way to get more precise measurements, as each point can be measured twice. In particular, this can be used to somewhat compensate for the effects of hysteresis.

Since this is the intended input for the PET, how the system responds to this type of signal is of interest. With the triangle signal needing to have a much higher frequency

than the ramp signal, the system response to triangle waves reveals much about what performance can be expected.

Results

Figure 4.12 shows the response of the PET system for different frequency triangle waves. A small ripple is visible at 5 Hz, while at 50 Hz the resulting movement is heavily distorted.

The distortion of the resulting displacement clearly shows the effects of exciting frequency components close to the resonance frequency of the tube. As the 50 Hz signal contains higher frequency components than the 5 Hz signal, the distortion is much greater.

This distortion clearly underlines the need for some form of control in order to achieve higher operating bandwidths for the PET, but that is not the topic of this thesis.
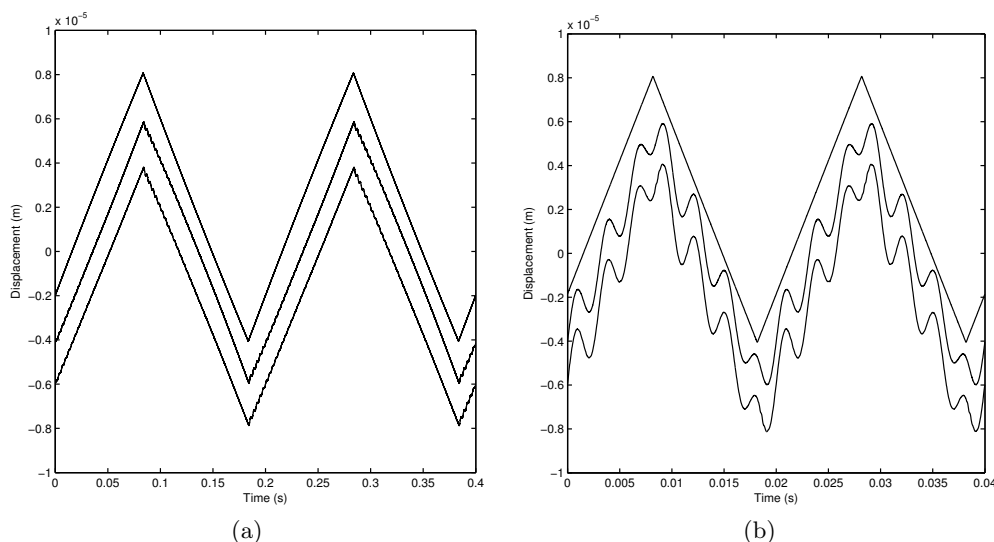

Figure 4.12: Plot of system responses for a triangle input of amplitude 80 V and frequency a) 5 Hz and b) 50 Hz. The responses are offset vertically for clarity. Responses from the top: Theoretical response $\tilde{d}$, Displacement registered by the capacitive sensor d_c, Displacement registered by the strain voltage sensor d_s.

4.7   Noise Levels

Introduction

The possible resolution of the PET is limited by both the resolution of the displacement itself and by the precision of the measurements. It is then interesting to see what precision levels can be achieved by the setup constructed for this thesis.

In this experiment the RMS (root mean square) value and the SD (spectral density) of the sensor noise levels were calculated. This was done by applying a zero volt signal to the system. The HIL controller has a sampling frequency of $10\,\text{kHz}$, and thus has a Nyquist/folding frequency of $5\,\text{kHz}$. In order to avoid aliasing, both the output voltages were filtered through the SRS SR560 Preamplifier set up as a first order RC low pass filter with cutoff frequency $3\,\text{kHz}$ and slope $12\,\text{dB/oct}$.. The HIL controller was used to record the outputs over a $5\,\text{s}$ period. This data was then scaled to represent the measured displacement, and the results plotted. The RMS and SD of the noise was then calculated in Matlab.

The RMS of a n length signal d is

$$RMS = \sqrt{\frac{1}{n}\sum_{i=1}^{n} x_i^2} \tag{4.23}$$

The SD of a signal is calculated as

$$SD = \frac{RMS}{\sqrt{w_k}} \tag{4.24}$$

where w_k is the bandwidth of the signal, in this experiment determined by the cutoff frequency of the applied lowpass filter.

Results

The noise plots are shown in Figure 4.13. The strain sensor noise looks to be lower than the capacitive sensor noise by a factor of approximately three.

The noise levels found are shown in Table 4.2. The results confirm that the strain voltage has a lower noise level than than the capacitive sensor. $3000\,\text{Hz}$ is a reasonable estimate for the bandwidth needed for high speed usage of the PET, and so the measured noise levels are good indicators of the precision available using the PET actuator setup constructed for this thesis.

Sensor	Noise RMS	Noise SD
Capacitive	$5.8574\,\text{nm}$	$106.94\,\text{pm}/\sqrt{\text{Hz}}$
Strain Voltage	$1.8801\,\text{nm}$	$34.33\,\text{pm}/\sqrt{\text{Hz}}$

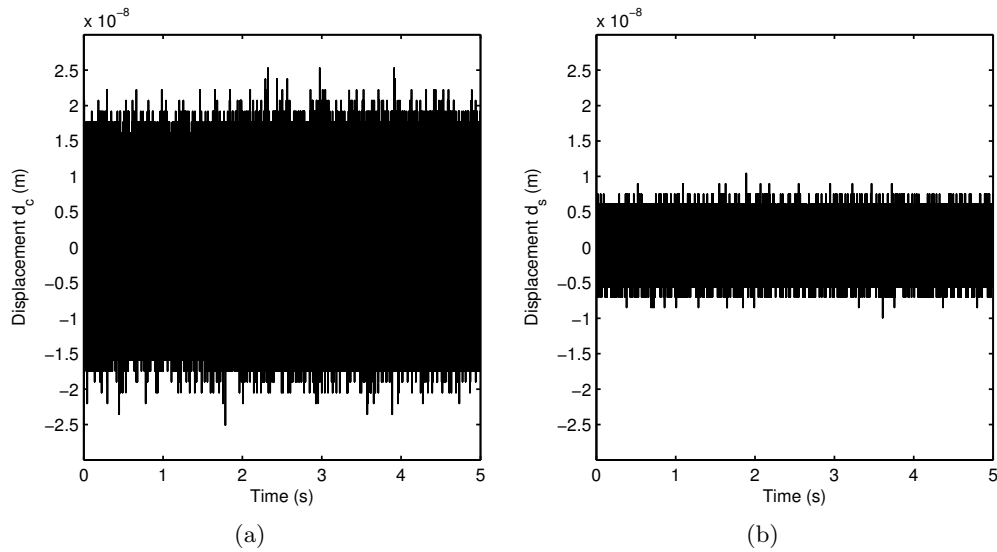Table 4.2: Measured sensor noise levels.

Figure 4.13: Displacement measurement noise of a) the capacitive sensor d_c and b) the strain voltage sensor d_s.

This result is only partially in agreement with findings from recent research on this subject. Fleming [10] also found the noise level of the strain voltage sensor to be lower than that of the capacitive sensor, but by a much bigger margin - approximately three orders of magnitude. This could be due to Fleming using a different electrical circuitry for the strain voltage sensor. Fleming also achieves a lower noise density for the capacitive measurement. It should be noted that while Fleming uses a specialized setup for doing the noise measurements, the results shown in this experiment was acquired using the standard HIL equipment that was used for all the experiments. It could be argued that while Fleming has found a theoretical resolution for the measurement techniques, the noise levels found in this experiment were the actual noise levels experienced during normal use of this PET setup.

4.8   Hysteresis

Introduction

A property of piezoelectric materials that has a significant impact on their behavior is a nonlinear hysteresis between the voltage applied and the displacement generated [2].

In order to analyze the hysteretic relationship between the applied voltage and the displacement, the PET was applied sinusoidal inputs of frequency $50\,\mathrm{Hz}$ and voltages $10\,\mathrm{V}$ and $80\,\mathrm{V}$ using the HIL controller. The resulting displacement was measured for one sine period using the capacitive sensor connected to the HIL controller. In Matlab, the input was plotted on the x axis against the measured displacement on the y axis.

Also, a triangular signal was applied with voltage $80\,\mathrm{V}$ and frequency $5\,\mathrm{Hz}$ using the HIL controller. The resulting displacement was also measured using the capacitive sensor. In Matlab, the output was plotted both against time and against the input signal u.
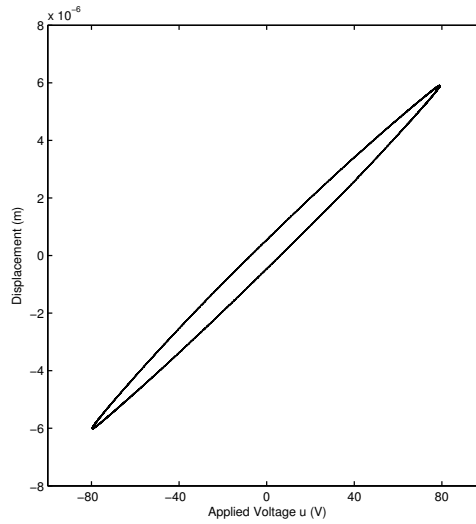
Results

The relationship between applied voltage and resulting measured displacement is shown in Figure 4.14. The results from applying $80\,\mathrm{V}$ show that the relationship between voltage and displacement is lower than a linear relationship in one area of the plot, and higher than linear on other parts. The lower than linear relationship happens at increasing voltage, while the higher than linear result happens at decreasing voltage.

This almost elliptical shape of the input-output plot could be due to both the inherent hysteresis of the material, or some time lag in the system. However, the plots for $80\,\mathrm{V}$ also show that the deviation from linear is largest close to $0\,\mathrm{V}$ and almost disappears close to $\pm80\,\mathrm{V}$. This suggests that there is more than just a time lag involved, since a pure time lag this would lead to a rounder shape close to the maximum applied voltage. At $10\,\mathrm{V}$, the noise component is more significant, while the hysteretic behavior looks to be noticeably smaller.

Figure 4.15 shows the measured displacement due to a triangular input over time, compared to the theoretical displacement found by using Chen's methods. Here it is shown even more clearly that the deviation from the linear relationship is at its largest close to $0\,\mathrm{V}$ and almost disappears close to the maximum voltage. Figure 4.16 shows the measured displacement as a function of the triangular input, and further confirms that the relationship is an example of nonlinear hysteresis. A pure lag component for the triangular input signal would result in a shape resembling a rotated rectangle.
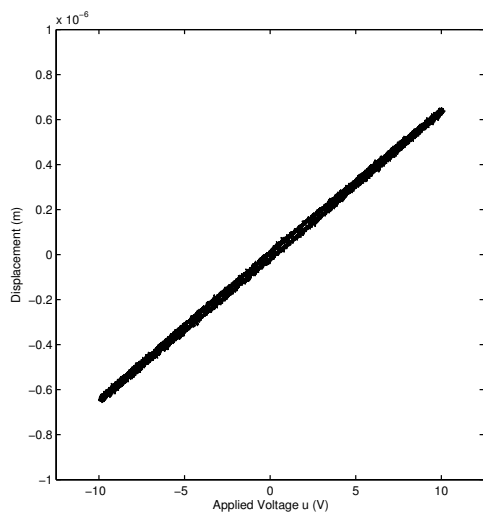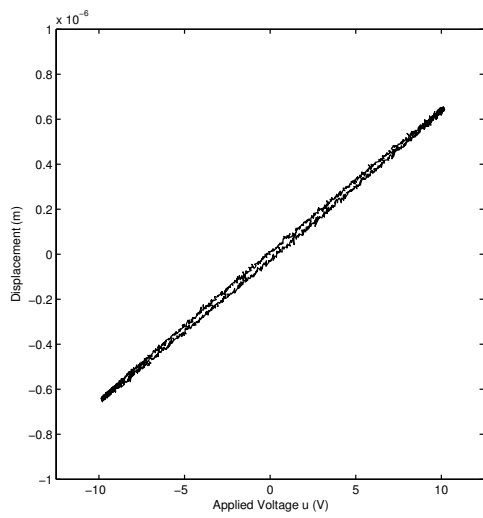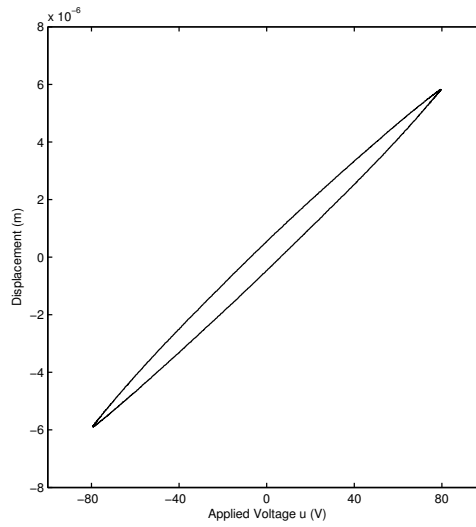
Figure 4.14: Plot of the relationship between applied sine wave voltage u of a) 10 V and b) 80 V and resulting displacement d_c measured by the capacitive sensor.
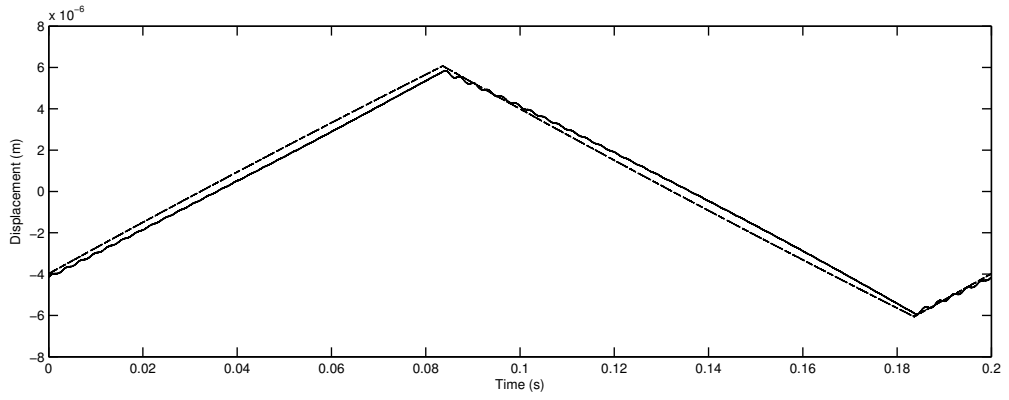
Figure 4.15: Plot of the displacement of the PET due to a triangular input on u as measured by the capacitive sensor d_c (solid line), compared to the theoretical displacement $\bar{d}$ as per Chen (stripes).
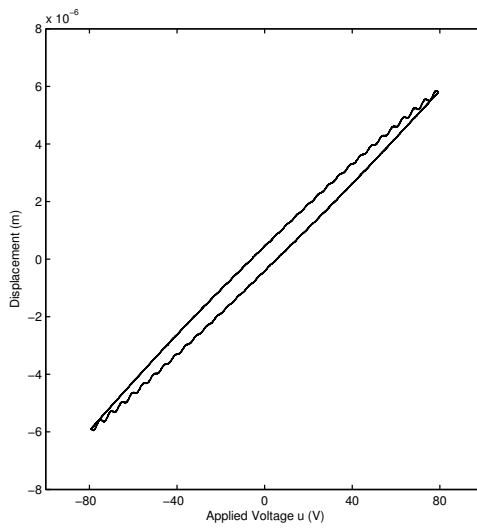

Figure 4.16: Plot of the relationship between an applied triangular input on u and the displacement d_c measured by the capacitive sensor.

4.9 Creep

Introduction

Creep is a property of piezoelectric actuators that can cause significant errors if not accounted for. When voltage is applied to a piezoelectric material, the piezoelectric effect is caused by the crystalline domains of the piezoelectric material becoming polarized and realigning. After a voltage change resulting in instantaneous displacement change, this realignment continues to happen for some time, resulting in displacement creep [19].

In order to demonstrate the piezoelectric creep effect, the HIL controller was used to apply a pulse signal of amplitude $0 - 80\,\mathrm{V}$ with a long period of $5\,\mathrm{s}$ to the PET input u. The resulting output displacement from the capacitive sensor was recorded along with the measured input voltage and plotted in Matlab.

Results

The applied voltage u and the measured displacement d_c is shown in Figure 4.17. In accordance with theory, while the input voltage reached a stable high level a short time after jumping from low to high, the displacement continued to creep slightly towards a steady state. The same effect is visible after the high-low flank, the displacement decreases gradually after the input voltage has stabilized.
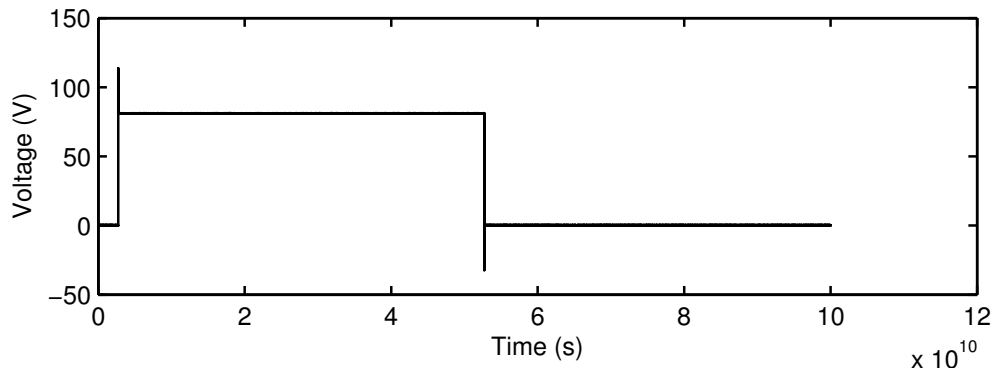
(a) Applied voltage u
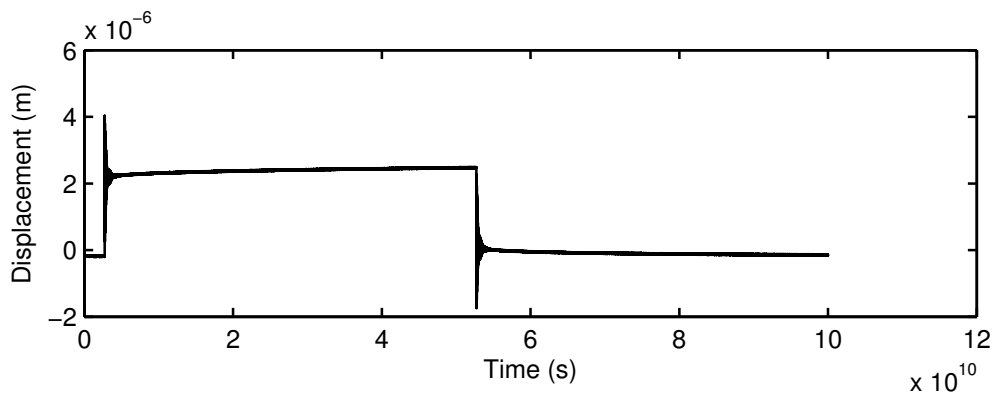
(b) Displacement measured by capacitive sensor d_c

Figure 4.17: Plot of the system response to a pulse signal with period 5 s, high amplitude 80 V and low amplitude 0 V.

4.10   Strain Voltage Drift

Introduction

As was shown in Section 4.7, the strain voltage sensor experience less noise than the capacitive sensor, and as seen in Section 4.4, the strain voltage does not exhibit the slight low-pass behavior of the capacitive sensor. This should provide for a much better resolution using the strain voltage measurement. However, as described in Section 3.6 the capacitive behavior of the sensor makes it inaccurate when low frequency signals are applied to the PET. In order to demonstrate this effect, the PET was applied a 5 s period pulse signal with 80 V amplitude, and the strain voltage sensor output was compared to the displacement measured by the capacitive sensor.
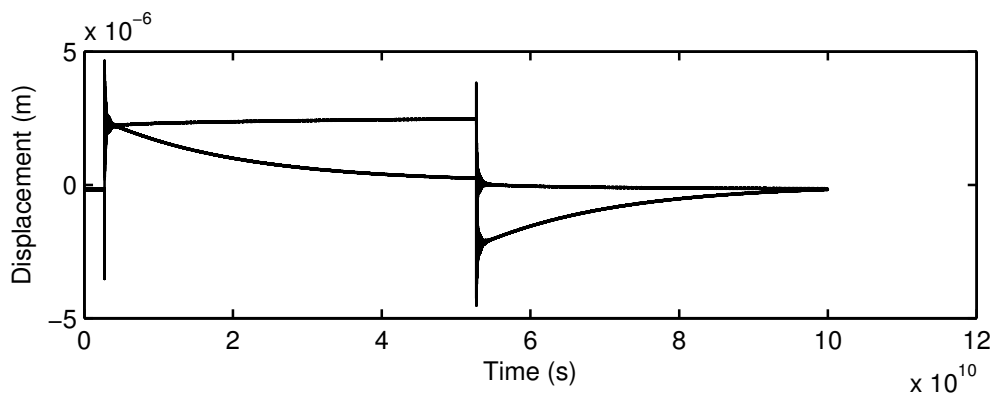
Results

Figure 4.18: Plot of the system response to a pulse signal with period 5 s, high amplitude 80 V and low amplitude 0 V. Dotted line is the displacement measured by the capacitive sensor d_c, solid line is the displacement measured by the strain voltage sensor d_s.

As seen in Figure 4.18, while the PET displacement shows a slight creep upwards, the strain voltage output seems to be exponentially approaching zero as soon as the step is completed. When then the PET displacement steps back down to zero, the strain voltage output jumps a corresponding level further down, before again approaching zero. This clearly demonstrates how the capacitive behavior of the sensor hampers its ability to correctly measure low frequency dynamics.

53

4.11   Sensor Fusion

Introduction

In Sections 4.7 and 4.10 it was found that while the strain voltage sensor has a lower noise level than the capacitive sensor, it experiences drift at lower frequencies. The capacitive sensor is not affected by this drift. Fleming et al. [10] has combined these two measurements to get a more precise estimate of the displacement of the PET, using the high frequency components of the strain voltage measurement and the low frequency components of the capacitive sensor. He named this technique sensor fusion. Using the same principle as in [10], in this experiment a combined measurement $\hat{d}$ was found.

Because of the drift at low frequencies of the strain voltage sensor, a high-pass filter $W_s(s)$ was applied to the measurement d_s. A low-pass filter $W_c(s)$ was applied to the capacitive sensor measurement d_c to compensate at the lower frequencies. In order to get an unbiased estimate of the displacement, the filters would need to comply with the equation

$$W_c(s) + W_s(s) = 1 \quad \forall \, s \tag{4.25}$$

The filters were chosen as first order high- and low-pass

$$W_c(s) = \frac{\omega_\alpha}{s + \omega_\alpha} \qquad W_p(s) = \frac{s}{s + \omega_\alpha} \tag{4.26}$$

where the cutoff frequency ω_α was set to $30\,\mathrm{Hz}$, after it being found to produce a good estimate. The filters are shown in Figure 4.20. This would give

$$W_c(s) + W_p(s) = \frac{\omega_\alpha}{s + \omega_\alpha} + \frac{s}{s + \omega_\alpha} = \frac{s + \omega_\alpha}{s + \omega_\alpha} = 1 \tag{4.27}$$
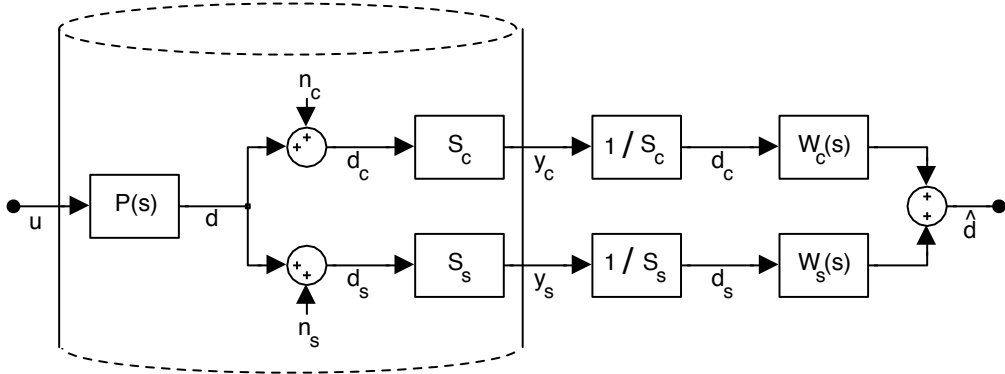
so (4.25) is fulfilled.

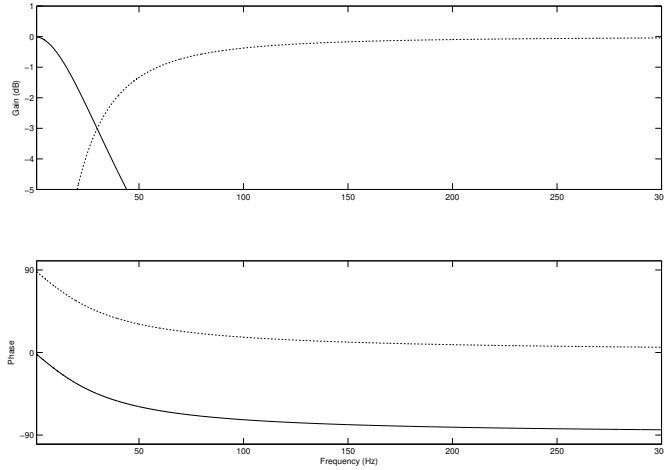Figure 4.19: Block diagram of the complete setup for sensor fusion.

Figure 4.20: Frequency response plots for the low- and high-pass filters $W_c(s)$ and $W_s(s)$.

A model of the full measurement system is shown in Figure 4.19. The equations for the combined displacement estimate $\hat{d}$ is then

$$
\begin{align}
\hat{d} &= W_c(s)d_c + W_s(s)d_s \tag{4.28} \\
&= W_c(s)(d + n_c) + W_s(s)(d + n_s) \tag{4.29} \\
&= (W_c(s) + W_s(s))d + W_c(s)n_c + W_s(s)n_s \tag{4.30} \\
&= d + W_c(s)n_c + W_s(s)n_s \tag{4.31}
\end{align}
$$

showing that the higher leveled noise from the capacitive sensor n_c is low pass filtered. Disregarding noise the expression becomes

$$
\hat{d} = d \tag{4.32}
$$

The relationship between the applied voltage and the combined displacement estimate was expressed as a transfer function

$$
\hat{P}(s) = \frac{\hat{d}}{u} \tag{4.33}
$$

which was found using the system identification techniques presented and used in Section4.5. The model order was set to be the same as for the individual sensor measurements.

In order to compare the combined displacement $\hat{P}(s)$ with the original measurements, the measured frequency response data for $G_c(s)$ and $G_s(s)$ was scaled to represent the measured relationship between applied voltage and displacement as shown in Section 4.4.

The frequency response data for the individual measurements were then plotted against the filtered and combined frequency response data. The combined measurement

was also plotted against the original measurements for a sine wave input of 5 Hz and 50 Hz and amplitude 80 V. Also, the frequency response data for $\hat{P}(s)$ was plotted against the found transfer function.

Results

The frequency response plots of $\hat{P}(s)$, $P_c(s)$ and $P_s(s)$ are shown in Figure 4.21. The frequency response of $\hat{P}(s)$ shows a peak of gain -118 dB at 332.4 Hz, and a gain of -146 dB with a small negative phase at the lower frequencies. It is seen that the combined estimate $\hat{P}(s)$ is closer to the capacitive displacement measurement at the lowest frequencies, and approaches the strain voltage displacement gradually towards 30 Hz. Around the resonant peak and for the high frequency band, $\hat{P}(s)$ is very close to $P_s(s)$. This is all in accordance with what could be expected. The combined estimate uses the capacitive measurements for the lowest bandwidths and the strain voltage measurements for everything else.

The PET displacement for a sine wave input as measured by each sensor and the combined estimate is shown in Figure 4.22. For the 5 Hz sine input, the combined estimate is close to the capacitive measurement. The noise level also looks to be similar to the capacitive sensors noise. For the 50 Hz input, the estimate is closer to the strain voltage estimate. The noise level is also lower than for the 5 Hz plot. This is in accordance with what Figure 4.21 shows, and with what Fleming finds in [10].

The model fitting the transfer function $\hat{P}(s)$ was found to be

$$\hat{P}(s) = \frac{-2.199 \times 10^{-9}s^2 - 1.733 \times 10^{-6}s + 0.2201}{s^2 + 78.24s + 4.468 \times 10^6} \tag{4.34}$$

Figure 4.23 shows the filtered and combined frequency response data for $\hat{P}(s)$ and the identified model for the transfer function. Overall the fit is pretty close. The somewhat negative phase of the data at low frequencies is not accounted for. At the peak the model has a slightly higher gain and the peak appears at a higher frequency. At high frequencies the the model closely follows the measurement data.
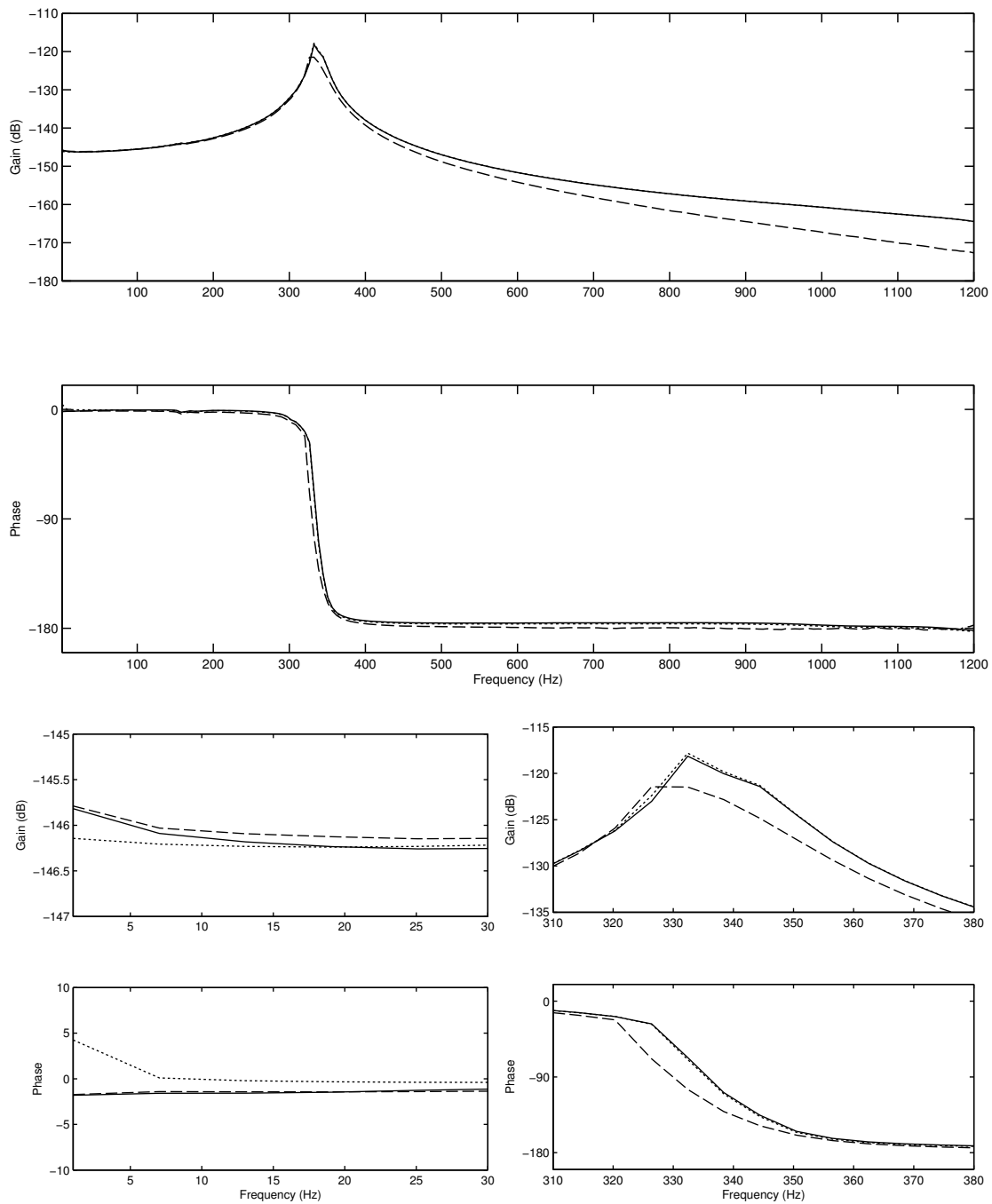
Figure 4.21: Frequency response plots of $\hat{P}(s)$ (solid), $P_c(s)$ (dashed) and $P_s(s)$ (dotted).

Figure 4.22: PET displacement to a sine wave input of amplitude 80 V and frequency a-b) 5 Hz and c-d) 50 Hz, as measured by the capacitive sensor (dashed), the strain voltage sensor (dotted) and as calculated in the combined measurement (solid line).

Figure 4.23: Frequency response plots of the measured, filtered and combined data for $\hat{P}(s)$ (dotted) and the found model (solid line).

Chapter 5

Evaluation

5.1   Summary of Results

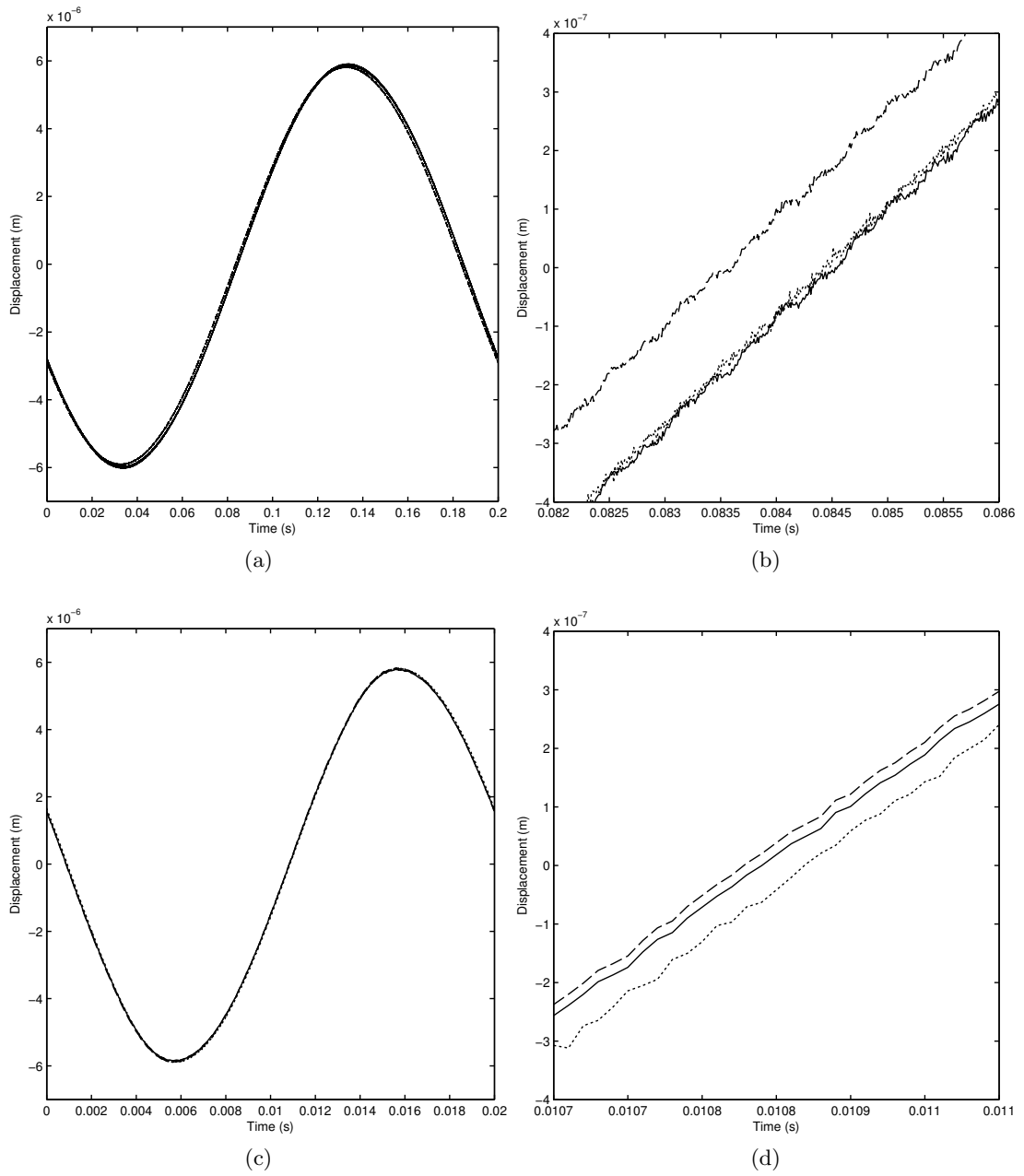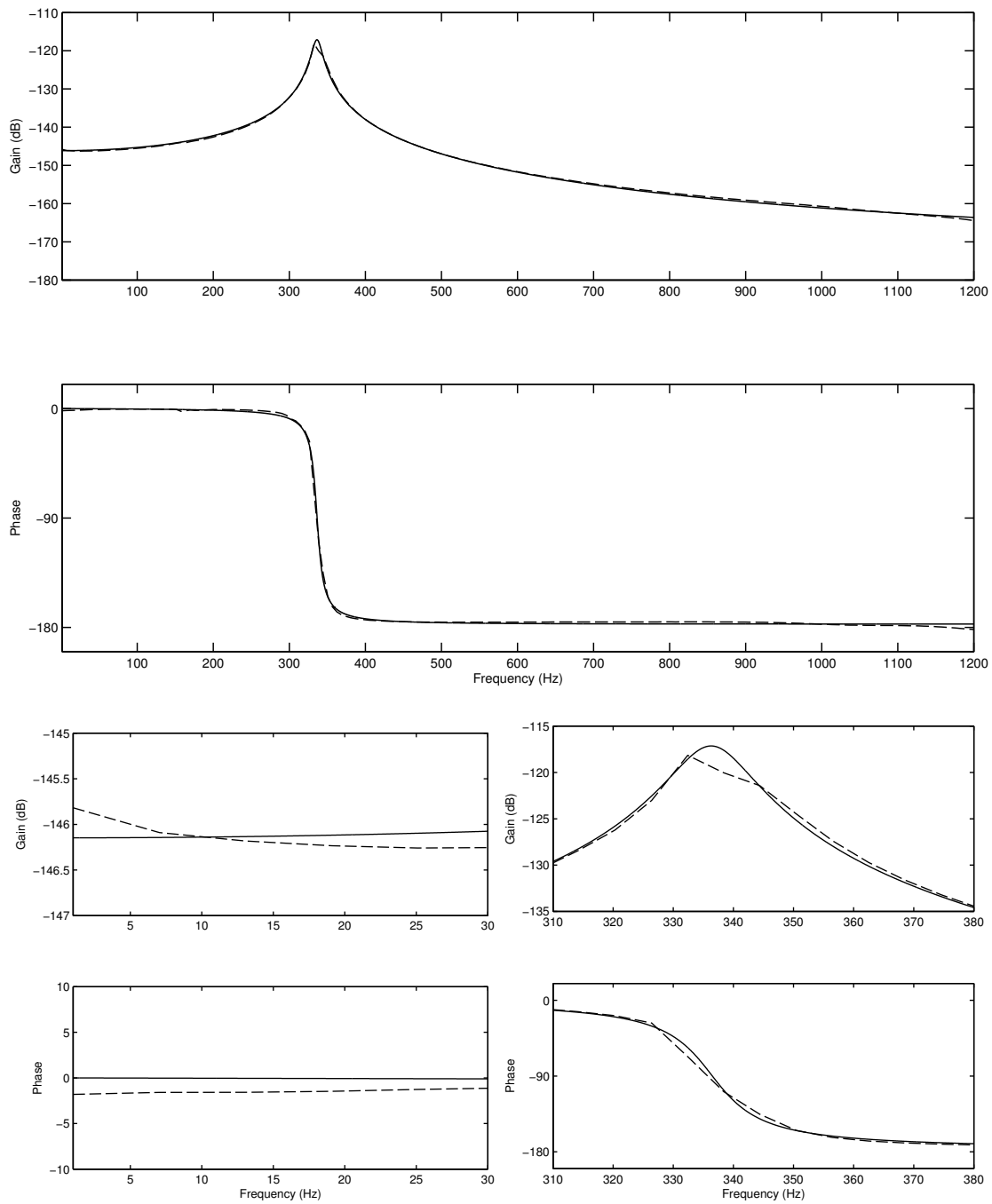This thesis presented a laboratory setup for actuating and measuring displacement of a piezoelectric tube. The setup was inspired by a setup used for several research papers on PETs, although some individual adjustments were made in order to suit the experiments conducted for the thesis. Then several experiments were conducted on the PET.

The capacitance of the PET was measured and found to be lower than was expected from theoretical calculations. This could be due to partial depoling of the piezoelectric material, something that could have occurred because of excess heat during soldering.

It was shown that the PET in most cases exhibit behavior closely matching what was expected from current literature on the subject. The frequency response measurements of the system showed that the PET has an underdamped harmonic resonance at 332.4 Hz. This frequency is significantly lower than what has been found by earlier research using similar equipment, and is assumed to be due to a relatively heavy capacitive target mounted to the free end of the PET. At higher frequencies the gain rolls off slowly, which is also to be expected. Second order linear models were identified from the frequency response data, and were shown to fit the measured data well.

The sensor noise was measured and found to be 1.8801 nm for the strain voltage measurement, which is about 3.6 times the size of a Cesium atom. This is a reasonable result given the equipment used, but it means that there still are improvements to be made in order to reach atomic resolution.

Nonlinear properties of the PET such as creep and hysteresis was demonstrated and briefly discussed, and the PET response to a triangular wave input was shown in order to emulate how the tube would react to common usage patterns. For this, significant distortion was shown at a frequency no higher than 50 Hz.

The strain voltage sensor was shown to have a lower noise level than the capacitive sensor but was shown to perform badly at low frequencies. Because of this a displacement measurement estimate was created by combining a high-pass filtered strain voltage measurement with a low-pass filtered capacitive measurement. This estimate was shown to exhibit both low noise and accuracy at low frequencies.

5.2 Sources of Error

5.2.1 Mechanical Noise

With the PET being a electromechanical system depending on the physical deflection of the tube, mechanical noise such as external vibrations could play a significant role in the measurements. The damping layer of the PET setup removed most of the observable mechanical noise, but the system still reacted slightly to external events such as doors slamming shut across the hall. This effect should be minimized further by mounting the PET on a commercial damping table instead of the impromptu solution used for this thesis.

5.2.2 Electrical Noise

The noise levels of the system were presented and discussed in Section 4.7. Noise will always be an issue in electrical and mechanical experiments, especially when the sizes to be measured are this small. Electrical noise can only be avoided to a certain degree, and the lower the noise level, the harder it is to reduce it further. Both 50 Hz noise from the mains and high frequency noise from surrounding electrical equipment can affect the performance of the PET. This is something that will be crucial in achieving even higher resolution that what was shown in this thesis.

5.2.3 Quantization

In order to analyze the measurements on the computer, the output voltages from the system were connected through analog/digital converters. Since computers have a finite resolution, this conversion will always involve some quantization error. Even so, the dSpace HIL controller used as an A/D-converter has a resolution of 16 bits. With a range of ± 10 V the available voltage resolution is then 0.3 mV, which means the quantization noise is lower than the noise level of the analog system.

5.2.4 Temperature Dependency

One cause for error is the temperature dependency of the piezoelectric properties of PZT. Temperature changes have been shown to significantly affect the piezoelectric constants [7], thus affecting both the relationship between applied voltage u and displacement d, and the relationship between d and the resulting strain voltage y_s. Anecdotal experience from the experiments conducted in this thesis also suggested a strong temperature dependency of these relationships.

To minimize the potential effects of temperature change, the temperature of the equipment and the environment was closely monitored during the experiments conducted, and kept close to 24 ∘c at all times. Additionally, the experiments were conducted over a short time span in order to maintain the same conditions for all the experiments.

5.3   Conclusion

This thesis has detailed the construction of a basic laboratory setup for actuation and nanometer displacement measurement of a piezoelectric tube. Both the needed specifications, the equipment employed, the electrical circuitry and the mechanical construction have been presented.

Through a series of experiments, the linear dynamics and nonlinear properties of the PET were identified, discussed and related to current literature. This included the frequency responses from applied voltage to displacement of the PET. Generally, the results that were found closely matched what has been found in similar research, although there were some notable differences, such as in gain and resonance frequency. Some of these differences were explained by differences in setup, while the source of others remain uncertain.

Both a capacitive sensor and a piezoelectric strain voltage sensor were utilized for measuring displacement, and the results were discussed and compared. It was found that the capacitive sensor had a higher noise level but was more accurate at lower frequencies than the strain voltage sensor. The two measurement were then combined into an improved estimate of the displacement of the PET.

The laboratory setup described in this thesis has largely been shown to be a reasonable setup for studies of piezoelectric tube actuators, and should provide a fine platform for continued research into the subject at NTNU.

5.4   Further Work

As the main aim of this thesis was to lay the foundation for further research into PETs, naturally there still are vast improvements to be made. Resolution is one aspect of the setup that could be improved, for instance by further minimizing the effects of noise components in the system. Both mechanical and electrical noise could probably be lowered significantly using relatively simple steps such as better dampening and electrical shielding.

The sensor fusion technique used in Section 4.11 is relatively simple, and improved results have been shown using more advanced filtering techniques such as Kalman filters for estimating the displacement [10]. This could be investigated further.

Lastly, this thesis does not discuss the topic of control. Various control schemes have been found to improve the properties of PETs drastically [12, 20, 13], and the sensors presented in this thesis could very well be used for techniques such as feedback control. This would be a natural next step for further research.

Appendix A

List of Equipment

Producer, Model	Serial No.
SRS SR560 Low Noise Preamplifier	96083
Solartron 1253A Frequency Response Analyzer	IF00023622
Trek PZD350 High Voltage Power Amplifier	150
ADE Technologies MicroSense II 6810 Gauging Module	11781
dSpace DS1103 PPC Controller Board	
SRS SIM965 Analog Filter	

Bibliography

[1] R. Zsigmondy, "Zur erkenntnis der kolloide: Über irreversible hydrosole und ultra-mikroskopie," p. 185, Jan 1905.

[2] B. Bhushan, "Springer handbook of nanotechnology," Jan 2006.

[3] G. Binnig, H. Rohrer, C. Gerber, and E. Weibel, "Surface studies by scanning tunneling microscopy," *Physical Review Letters*, vol. 49, pp. 57–61, Jan 1982.

[4] G. Binnig, C. Quate, and C. Gerber, "Atomic force microscope," *Physical Review Letters*, vol. 56, pp. 930–934, Jan 1986.

[5] S. Moheimani, "Invited review article: Accurate and fast nanopositioning with piezoelectric tube scanners: Emerging trends and future challenges," *Review of Scientific Instruments*, vol. 79, Jan 2008.

[6] S. Aphale, B. Bhikkaji, and S. Moheimani, "Minimizing scanning errors in piezoelectric stack-actuated nanopositioning platforms," *Nanotechnology*, vol. 7, pp. 79–90, Jan 2008.

[7] D. Wang, Y. Fotinich, and G. Carman, "Influence of temperature on the electromechanical and fatigue behavior of piezoelectric ceramics," *Journal of Applied Physics*, Jan 1998.

[8] G. Binnig and D. Smith, "Single-tube three-dimensional scanner for scanning tunneling microscopy," *Review of Scientific Instruments*, vol. 57, pp. 1688–1689, Jan 1986.

[9] S. Devasia, E. Eleftheriou, and S. Moheimani, "A survey of control issues in nanopositioning," *Control Systems Technology*, vol. 15, pp. 802 – 823, Sep 2007.

[10] A. Fleming, A. Wills, and S. Moheimani, "Sensor fusion for improved control of piezoelectric tube scanners," *Control Systems Technology*, vol. 16, pp. 1265 – 1276, Nov 2008.

[11] C. Chen, "Electromechanical deflections of piezoelectric tubes with quartered electrodes," *Applied Physics Letters*, vol. 60, pp. 132–134, Jan 1992.

[12] M. Ratnam, B. Bhikkaji, A. Fleming, and S. Moheimani, "Ppf control of a piezo-electric tube scanner," *Decision and Control*, Jan 2005.

[13] I. Mahmood, K. Liu, and S. Moheimani, "Two sensor based h∞ control of a piezo-electric tube scanner⋆," *Proceedings of the 17th World Congress*, pp. 8251–8256, 2008.

[14] S. Moheimani and Y. Yong, "Simultaneous sensing and actuation with a piezoelectric tube scanner," *Review of Scientific Instruments*, Jan 2008.

[15] B. Bhikkaji, M. Ratnam, A. Fleming, and S. Moheimani, "High-performance control of piezoelectric tube scanners," *IEEE Transactions on Control Systems Technology*, Jan 2007.

[16] J. Maess, A. Fleming, and F. Allgower, "Simulation of piezoelectric tube actuators by reduced finite element models for controller design," *Proc. American Control Conf.*, pp. 4221–4226, Jan 2007.

[17] D. Croft, G. Shed, and S. Devasia, "Creep, hysteresis, and vibration compensation for piezoactuators: Atomic force microscopy . . . ," *Journal of Dynamic Systems*, vol. 123, pp. 35–43, Jan 2001.

[18] L. Ljung, "System identification: Theory for the user," *Prentice-Hall*, Jan 1987.

[19] H. Georgiou and R. Mrad, "Dynamic electromechanical drift model for pzt," *Mechatronics*, Jan 2007.

[20] A. Fleming, "A new robust damping and tracking controller for spm positioning stages," *Unpublished*, Sep 2008.